water

MDPI

Article

Mechanical Properties and Microstructural Evolution of Dispersive Soils Under Freeze–Thaw Cycles

Xingchao Liu [1], Xionglong Zhang [1], Jiangjiang Shen [1], Yangming Zhang [1], Renhui Guan [2], Qixun Lv [2], Enliang Wang [1,3,*], Liqiang Wang [2,*], Haiqiang Jiang [1,3] and Hongwei Han [1,3]

[1] College of Hydraulic Science and Engineering, Northeast Agricultural University, Harbin 150030, China; dnlxc@neau.edu.cn (X.L.); 18955646170@163.com (X.Z.); 18993445949@163.com (J.S.); zym2621567744@163.com (Y.Z.); hqjiang@neau.edu.cn (H.J.); hanhongwei@neau.edu.cn (H.H.)
[2] Heilongjiang Provincial River Regulation Engineering Construction Management Co., Ltd., Harbin 150090, China; 18845779492@163.com (R.G.); 18345378986@163.com (Q.L.)
[3] Heilongjiang Provincial Key Laboratory of Water Resources and Water Conservancy Engineering in Cold Region, Northeast Agricultural University, Harbin 150030, China
* Correspondence: wel@neau.edu.cn (E.W.); 18246144647@163.com (L.W.)

Abstract

Dispersive soils are widely distributed in the seasonally frozen regions of northeastern China, where hydrothermal dynamics driven by seasonal freeze–thaw (FT) cycles dominate the hydrological evolution and mechanical deterioration of soil masses, posing a serious threat to the long-term stability of hydraulic engineering in cold regions. However, the hydro–thermo–mechanical (HTM) coupled degradation mechanisms of dispersive clay from the South Nenjiang Main Canal remain poorly understood, particularly the linkage between FT-induced microstructural evolution and macroscopic mechanical behavior. In this study, low-plasticity dispersive clay specimens were subjected to 0–12 FT cycles. Unconsolidated undrained (UU) triaxial tests were conducted to evaluate mechanical behavior, while scanning electron microscopy (SEM) combined with the Pore and Crack Analysis System (PCAS) was used to quantify microstructural evolution. Results indicated that increasing FT cycles transformed the stress–strain response from mild strain-softening to strain-hardening, with the failure mode evolving toward bulging-type ductile failure. Cohesion exhibited a pronounced exponential decay, with the most significant degradation occurring within the first three FT cycles and stabilizing after approximately six FT cycles, whereas the internal friction angle showed only minor variation. At the microscale, porosity and total pore area increased continuously through micropore coalescence and macropore development, with a slight decrease in fractal dimension indicating reduced pore boundary complexity and smoothed pore interfaces due to frost heave-induced pore merging. The FT-induced hydrothermal disturbance promoted pore-water phase transition and redistribution, resulting in progressive pore enlargement and loss of structural integrity. Because the specimens were tested in sealed, closed-system conditions with a nearly constant total water content, this degradation chain is attributable specifically to in situ ice–water phase transitions and internal pore-water redistribution, i.e., water-phase-change-driven processes, rather than to external water supply. It is demonstrated that interparticle bond breakage and pore expansion–coalescence driven by ice–water phase transitions dominate strength degradation, promoting a transition from structure-dominated to friction-dominated strength behavior. A normalized cohesion reduction factor and a cohesion degradation index are further proposed to quantify the progressive loss of structural integrity and to provide a design-oriented tool for cold-region geotechnical practice. These findings provide a basis for stability assessment and hazard mitigation of dispersive soils in cold-region engineering.

Check for updates

Academic Editor: Zhuotong Nan

Received: 24 July 2026
Revised: 30 August 2026
Accepted: 30 August 2026
Published: 31 August 2026

Copyright: © 2026 by the authors. Licensee MDPI, Basel, Switzerland. This article is an open access article distributed under the terms and conditions of the Creative Commons Attribution (CC BY) license.

Keywords: dispersive soil; freeze–thaw cycles; shear strength; ice–water phase transition; microstructure; cohesion reduction model; degradation index

1. Introduction

Dispersive soils represent a special class of cohesive soils with extremely poor engineering and hydrological properties. Owing to their high sodium adsorption ratio (SAR) and exchangeable sodium percentage (ESP), their flocculated structure is inherently unstable and readily disintegrates into individual colloidal particles when exposed to low-salinity or distilled water, resulting in a rapid loss of shear strength upon wetting [1–3]. Under seepage conditions, such characteristics make dispersive soils highly vulnerable to erosion, piping, and internal instability, posing significant threats to the long-term safety of hydraulic engineering structures, including earth dams and canal embankments [4,5]. Dispersive soils are widely distributed in Australia, the United States, South Africa, as well as northeastern and northwestern China [6,7]. Inadequate identification and remediation during site investigation and construction may trigger severe erosion, slope instability, and even catastrophic structural failure, incurring substantial economic losses and adverse environmental impacts.

Accurate identification and effective stabilization of dispersive soils have long been core research priorities in geotechnical and hydraulic engineering. At present, the assessment of soil dispersivity primarily relies on physical methods, including the pinhole test, double hydrometer test, and crumb test, often combined with chemical indices such as ESP and SAR for comprehensive evaluation [5,8,9]. In engineering practice, traditional chemical stabilization methods commonly employ cementitious additives such as alum, lime, cement, and fly ash to mitigate soil dispersivity and enhance strength through cation exchange and cementation mechanisms [10–12]. In recent years, driven by the demand for sustainable development and resource recycling, increasing attention has been directed toward industrial by-products (e.g., slag, silica fume, and recycled concrete powder) [13–15] and bio-based materials (e.g., lignin and xanthan gum) [16,17] as environmentally friendly alternatives to conventional high-energy-consumption stabilizers. Moreover, nanomaterials (e.g., nano-silica and nanoclay), owing to their high specific surface area and strong ion exchange capacity, have also been explored to improve the engineering properties of dispersive soils [18,19]. Nevertheless, the majority of available studies only focus on optimizing the inherent physical and mechanical properties of dispersive soils, while the long-term deterioration behaviors under complex environmental conditions, particularly cold-region freeze–thaw environments, have not been thoroughly explored.

Notably, the regions with concentrated dispersive soil distribution in China—Northeast China, Northwest China, and the Qinghai–Tibet Plateau—are all typical seasonally frozen ground regions, where FT cycles constitute a dominant environmental force controlling soil hydrothermal evolution and engineering performance. From theHTM coupling perspective, FT cycling can be regarded as cyclic thermal loading induced by seasonal temperature fluctuations. During this process, pore water undergoes repeated ice–water phase transitions accompanied by latent heat exchange and a volumetric expansion of approximately 9% upon freezing [20]. The frost heave stresses generated consequently exert mechanical disturbance on the soil skeleton, facilitating particle rearrangement, degradation of intergranular bonds and irreversible structural deterioration. From a hydrological perspective, FT cycling is fundamentally a soil–water interaction process: pore water acts both as the medium of thermal transport and as the active agent that transmits phase-change-induced forces to the soil skeleton. Moreover, the water-supply condition strongly controls the FT

degradation process: in open systems, external water migrates toward the freezing front and intensifies frost heave, whereas in closed systems, degradation is driven exclusively by the phase change and internal redistribution of the initially available pore water. Numerous studies have demonstrated that FT cycles significantly alter soil microstructure, pore distribution, and mechanical properties [21–23]. Qi et al. [21] systematically reviewed the effects of FT cycles on soil engineering properties. They reported that FT action exerts a loosening effect on dense soils and a densification effect on loose soils. The most pronounced effect occurs during the first FT cycle. Wang et al. [24] found that after 21 FT cycles, the elastic modulus and failure strength of Qinghai–Tibet clay decreased significantly, with cohesion continuously declining while the internal friction angle slightly increased. Yang et al. [25], based on triaxial shear tests of FT-treated specimens, observed that the elastic modulus, cohesion, and internal friction angle all exhibited decreasing trends with increasing FT cycles. Zheng et al. [26] noted that the cohesion of loess decreased after FT cycles and stabilized after approximately five cycles, whereas the internal friction angle was less sensitive to FT effects; meanwhile, the structure of remolded loess became progressively looser after FT cycles. Recent studies have further extended these findings to different soil types and coupled environmental conditions. Guo et al. [27] reported that the shear strength of silty clay subjected to coupled dry–wet–freeze–thaw cycles decreased with increasing cycle number and stabilized after approximately six cycles. Yang et al. [28] observed progressive strength loss in geogrid-reinforced expansive soil under FT cycling, while similar degradation trends have been reported for shallow Ili loess [22] and black soils in northeastern China [23]. Overall, FT cycles commonly lower soil shear strength and cohesion, while the variation trend of internal friction angle varies significantly among different soil types and has not reached a unified conclusion.

Extensive research has been conducted worldwide on dispersive soils in seasonally frozen ground regions. Existing findings indicate that FT cycles further exacerbate the deterioration of dispersive soils, manifested by alterations in unsaturated hydraulic characteristics and reduced erosion resistance [19,29]. Zhang et al. [30] reported that after FT cycles, the unconfined compressive strength (UCS) of dispersive soils decreased significantly, accompanied by increased porosity and crack density, thereby accelerating structural degradation and strength loss. Zhang and Han [31] further confirmed through triaxial tests and SEM analyses that the failure strength of dispersive soils is negatively correlated with porosity, mean pore diameter, and shape factor. Increasing FT cycles lead to enlarged pore parameters and progressive weakening of interparticle bonding. Despite these advances, the underlying mechanisms governing FT cycle-induced deterioration in dispersive soils remain inadequately understood, particularly in terms of the coupling between microstructural evolution and macroscopic mechanical response. More critically, the coupled effects of FT-induced thermal disturbance, ice–water phase transitions, and pore structural evolution on microscale damage accumulation and macroscopic mechanical degradation have not been systematically clarified. In addition, although advanced characterization techniques such as mercury intrusion porosimetry (MIP), nuclear magnetic resonance (NMR), and X-ray computed tomography (XCT) have been used to quantify FT-induced pore evolution in various soils [23,32], and previous studies have correlated pore parameters with the failure strength of dispersive soils [31], the mechanisms linking FT-induced pore structural evolution to the degradation of shear strength parameters (e.g., cohesion) of dispersive soils have not been systematically clarified. Moreover, pronounced spatial variability in soil properties across different geographical regions further limits the generalization of existing findings. Consequently, systematic investigations into the mechanical behavior and microstructural characteristics of dispersive soils from the South Nenjiang Main Canal are still lacking.

To investigate the mechanical behavior and microscale deterioration mechanisms of dispersive soils, soil samples were collected from the slope of the South Nenjiang Main

Canal (a key component of the South Nenjiang Water Diversion Project), located in a representative seasonally frozen ground region of northeastern China. UU triaxial shear tests and SEM–PCAS image analyses were conducted on specimens subjected to 0–12 FT cycles under confining pressures of 100–300 kPa. For the microstructural characterization, vacuum freeze-dried specimens were examined with the SEM at a magnification of 1000×, and the acquired images were quantitatively processed using the PCAS system to extract areal porosity, total pore area, pore count, mean pore area, and pore fractal dimension, which jointly characterize the evolution of porosity and pore-size distribution; in addition, particle orientation and arrangement, including the evolution of interparticle contact modes (face-to-face, point-to-face, and point-to-point), were identified from the SEM images to link particle-scale fabric changes to the macroscopic mechanical response. Specifically, this study aims to: (i) characterize the FT-induced evolution of the stress–strain response, failure strength, and shear strength parameters; (ii) quantify the corresponding evolution of pore structure; (iii) establish a micro–macro correlation framework that links pore-scale evolution to macroscopic strength and identify the governing HTM degradation mechanism; and (iv) propose an empirical cohesion reduction model and a degradation index for engineering design. The principal novelty of this study lies in three aspects: (i) it provides a systematic micro–macro coupled characterization of FT-induced degradation of dispersive clay from the South Nenjiang Main Canal, where such coupled data were previously lacking; (ii) it links pore-scale indices to macroscopic strength parameters within a mechanistic micro–macro correlation framework; and (iii) it proposes a design-oriented cohesion reduction factor and a degradation index, advancing the current state of knowledge from qualitative descriptions of FT-induced damage toward a quantitative, design-ready framework for dispersive soils in cold regions. The findings provide theoretical references for stability evaluation, erosion prevention, and long-term service performance assessment of dispersive-soil hydraulic infrastructures in seasonally frozen regions. The proposed cohesion reduction factor $Rc(N)$ and degradation index $Dc(N)$ allow engineers to estimate the post-FT cohesion of dispersive soils directly from the initial strength parameters for incorporation into slope-stability calculations and preliminary design of canal embankments, while the quantified FT-dependent strength loss provides a basis for erosion-risk evaluation, safety assessment, and maintenance planning of dispersive-soil hydraulic infrastructures in seasonally frozen regions. Moreover, this study bridges soil mechanics and hydraulic engineering by addressing the water-phase-transition-driven degradation of soils beneath cold-region hydraulic structures, providing mechanistic insights and quantitative evidence for the safety and serviceability of water-related infrastructure.

2. Materials and Methods

2.1. Materials

The dispersive soil used in this study was collected from the South Nenjiang Main Canal in Daqing, Heilongjiang Province, China, with a sampling depth of 20–40 cm. The sampling location is shown in Figure 1. Our previous study confirmed that soils in this region exhibit high dispersivity [16], and field investigations revealed distinct erosion features on the slope surfaces. To provide direct experimental evidence for the dispersivity of the soil tested in the present work, standard dispersivity identification tests were conducted in accordance with ASTM D4647/D4647M-13 (pinhole test) [33] and ASTM D6572-21 (crumb test) [34]. The pinhole test was conducted under a 50 mm head of distilled water. After 5 min, the effluent became dark and turbid, the initial 1.0 mm diameter pinhole enlarged to approximately 4.0 mm, and the flow rate reached 1.5 mL/s, indicating that the soil was highly dispersive (Figure 2). The crumb test produced a profuse cloud of suspended clay colloids across the entire bottom of the dish, corresponding

to Grade 4 (Highly Dispersive) (Figure 3). The particle size distribution of the soil was determined using a laser particle size analyzer (OMEC SL-909, Zhuhai, China, Figure 4a), and the results are presented in Figure 4b. Following the conventional particle-size definition adopted in ASTM D2487-17(2025) [35], the soil consists of 1.76% clay-sized particles ($d \leq 0.002$ mm), 85.91% silt-sized particles ($0.002 \text{ mm} < d \leq 0.075$ mm), and 12.33% sand-sized particles ($0.075 \text{ mm} < d \leq 2$ mm). In addition, the basic physical properties and soluble salt composition of the soil were measured in accordance with Chinese standard GB/T 50123-2019 [36]. The corresponding test procedures are comparable to those specified in ASTM D2216-19 [37] for water content, ASTM D4318-17e1 [38] for Atterberg limits, and ASTM D698-12(2021) [39] for compaction characteristics. The results are summarized in Tables 1 and 2. Based on the ASTM D2487-17(2025) [35], the soil is classified as low-plasticity clay (CL). It should be noted that the USCS clay designation is based on the plasticity characteristics of the fine fraction rather than on the clay-sized particle content; the dispersive behavior of the tested soil is governed by its physicochemical properties rather than by grain-size composition alone. No X-ray fluorescence (XRF), X-ray diffraction (XRD), or EDX/EDAX analysis was performed in the present experimental campaign; therefore, the discussion of FT-induced microstructural change is intentionally restricted to morphology, pore geometry, and particle-contact characteristics rather than unsupported mineralogical or elemental transformations.

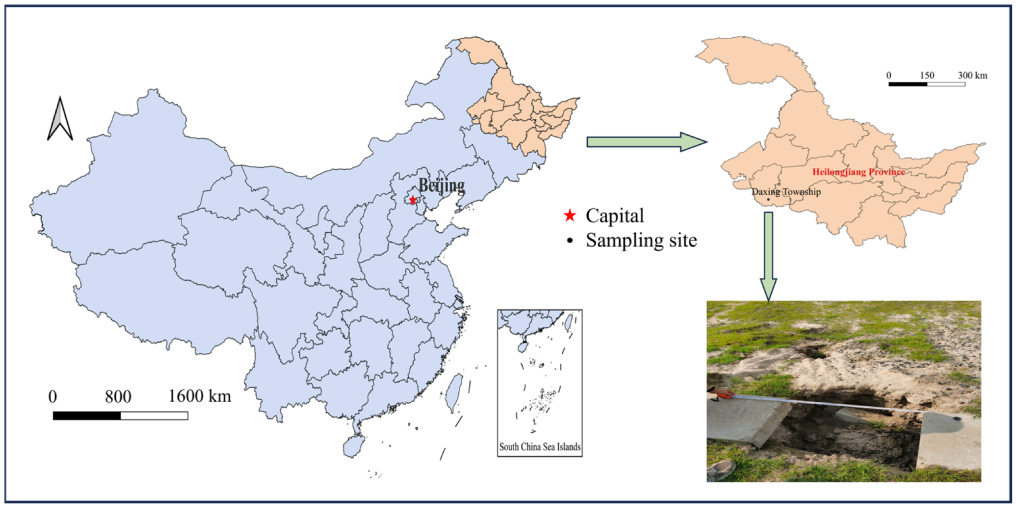
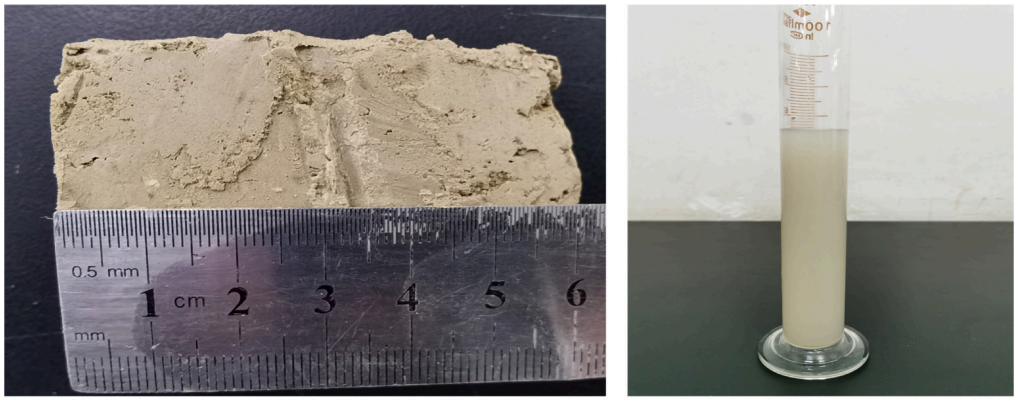
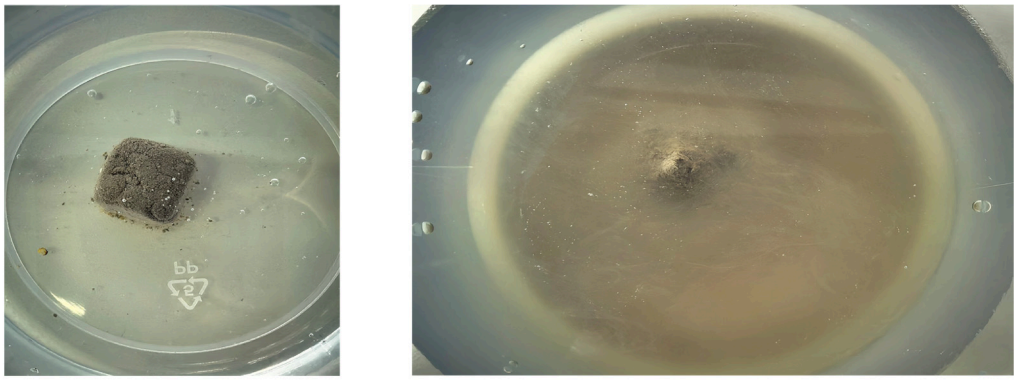


Figure 1. Sampling locations and slope erosion morphology.



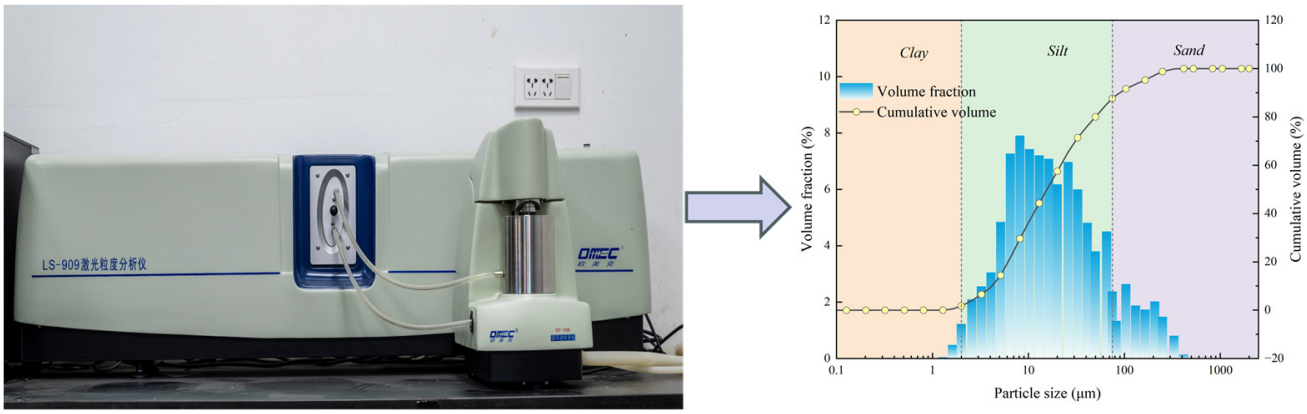
(a) (b)

Figure 2. Pinhole test. (**a**) Soil block specimen subjected to pinhole erosion; (**b**) dark-colored colloidal.



(a) (b)

Figure 3. Crumb test. (**a**) Soil crumb specimen at the beginning of immersion; (**b**) dense colloidal cloud formed after immersion.



(a) (b)

Figure 4. Particle analysis equipment and soil particle grading curve: (**a**) LS-909 laser particle size analyzer; (**b**) volume fraction and cumulative volume particle size distribution of soil.

Table 1. Basic physical properties of the soil.

Natural Moisture Content (%)	Particle Relative Density (g/cm^3)	Liquid Limit (%)	Plastic Limit (%)	Plasticity Index	Maximum Dry Density (g/cm^3)	Optimum Moisture Content (%)
16.5	2.62	29.57	17.39	12.18	1.77	16.8

Table 2. Basic chemical indexes of the soil.

Total Soluble Salt Content (%)	Individual Ion Contents (cmol/kg)						
0.41	CO_3^{2-}	HCO_3^-	Cl^-	SO_4^{2-}	Ca^{2+}	Mg^{2+}	Na^+
	1.1890	1.4456	0.3521	0.2487	0.1289	0.1753	2.9313

2.2. Specimen Preparation

The specimen preparation procedure followed the Standard for Geotechnical Testing Method (GB/T 50123-2019) [36], as illustrated in Figure 3.

The collected soil samples were first air-dried under laboratory conditions (Figure 5a,b) and then crushed on a rubber plate using a soil crusher and a stainless steel roller (Figure 5c). The crushed soil was passed through a 2 mm sieve (Figure 5d), and the passing fraction was oven-dried to remove residual moisture (Figure 5e). Distilled water was added incrementally to the dry soil and thoroughly mixed to achieve the optimum moisture content

of 16.8% (Figure 5f). The prepared soil was then sealed in plastic bags and allowed to equilibrate for 24 h (Figure 5g).



Figure 5. Specimen preparation procedure.

Cylindrical specimens (39.1 mm in diameter and 80.0 mm in height, i.e., a height-to-diameter ratio of approximately 2.0, which is the ratio recommended for triaxial testing) were statically compacted in five equal layers using a dedicated compaction apparatus (Figure 5h). The mold diameter of 39.1 mm corresponds to the standard triaxial specimen size specified in GB/T 50123-2019 [36] and matches the triaxial cell of the TSZ-1 strain-controlled triaxial system; accordingly, the 39.1 mm mold was used instead of the 40 mm mold commonly employed in other testing systems, and the specimen height of 80.0 mm was adopted to satisfy the preferred H/D = 2.0 requirement. The degree of compaction was strictly controlled at 0.95 (i.e., 95% of the standard Proctor maximum dry density) to guarantee specimen reproducibility and uniform initial fabric. To control and verify the target degree of compaction of 0.95, the moist soil mass required for each specimen was calculated from the target dry density (ρ_d = 0.95 × $\rho_{d,max}$ = 0.95 × 1.77 g/cm^3 = 1.68 g/cm^3), the specimen volume (approximately 96.1 cm^3), and the compaction moisture content (16.8%), and the pre-weighed soil

was divided into five equal portions for the five compaction layers. After demolding, the actual diameter and height of each specimen were measured with a vernier caliper at three locations, and the wet mass was recorded to determine the bulk density; the moisture content of representative trimmings was determined by oven-drying at 105–110 °C to constant mass in accordance with ASTM D2216-19 [37], and the dry density of each specimen was then calculated. The measured dry density of every accepted specimen was required to be within ± 0.01 g/cm^3 of the target value (1.68 g/cm^3), corresponding to a degree of compaction of 0.95 ± 0.006; specimens outside this tolerance were discarded and re-compacted. The maximum dry density and optimum moisture content used as reference values were obtained from the standard Proctor compaction test following GB/T 50123-2019 [36] and ASTM D698-12(2021) [39]. Upon demolding, the specimens were immediately sealed with multiple layers of plastic film to prevent moisture loss, labeled, and cured in a humidistat container for 48 h to facilitate internal moisture homogenization (Figure 5i).

All specimens were tested in their as-compacted, unsaturated state without post-compaction saturation or back-pressure consolidation prior to FT cycling. This specimen-preparation protocol follows the procedures reported in previous FT studies on cohesive soils [26,30].

2.3. The Test Scheme

2.3.1. FT Cycling Tests

To investigate the mechanisms underlying the deterioration of strength properties in dispersive soil during FT cycling, the prepared specimens were subjected to controlled FT cycling in the laboratory. Because existing freeze–thaw testing standards provide general guidance but do not prescribe a universally applicable combination of thermal conditions and cycle duration for all soil types and field conditions [40,41], the FT experimental parameters were determined by combining local field conditions with empirical evidence. The air temperature series over the past 20 years in Daqing City were first extracted from the ERA5-Land reanalysis dataset (available at https://cds.climate.copernicus.eu/, accessed on 13 May 2025); monthly mean values were then derived from these series and are presented in Figure 6a. From a thermodynamic perspective, the selected temperature range encompasses the conditions required to induce repeated pore-water freezing and thawing in low-plasticity dispersive clays, thereby promoting ice–water phase transitions and associated hydrothermal responses. Accordingly, a freezing temperature of −20 °C and a thawing temperature of 25 °C were chosen to simulate the extreme seasonal temperature fluctuations under natural field conditions in Daqing. Each complete cycle lasted 24 h, with 12 h freezing and 12 h thawing (Figure 6b). The same programmed temperature profile was applied to all specimens and throughout all FT cycles. Thus, the cooling and warming processes were controlled consistently, and the freezing/thawing rate was not treated as an independent experimental variable in this study. The 12 h duration assigned to each phase allows sufficient release and absorption of phase-change latent heat, facilitates complete freezing–thawing processes, and minimizes hydrothermal response hysteresis caused by rapid temperature fluctuations.

To ensure a constant moisture content and to eliminate external water supply, thereby minimizing net water migration across the specimen boundaries, all specimens were sealed in a double-layer configuration during FT cycling. Each specimen was first wrapped with plastic cling film and then placed in a heat-sealed polyethylene bag. Pre-liminary verification demonstrated that this sealing approach limited moisture content fluctuation to less than 0.2% over 12 FT cycles, ensuring the entire test was conducted un-der a closed-system condition. This experimental configuration enabled the intrinsic effects of in situ

ice–water phase transition and microscale pore-water redistribution on soil microstructural evolution and mechanical degradation to be evaluated.

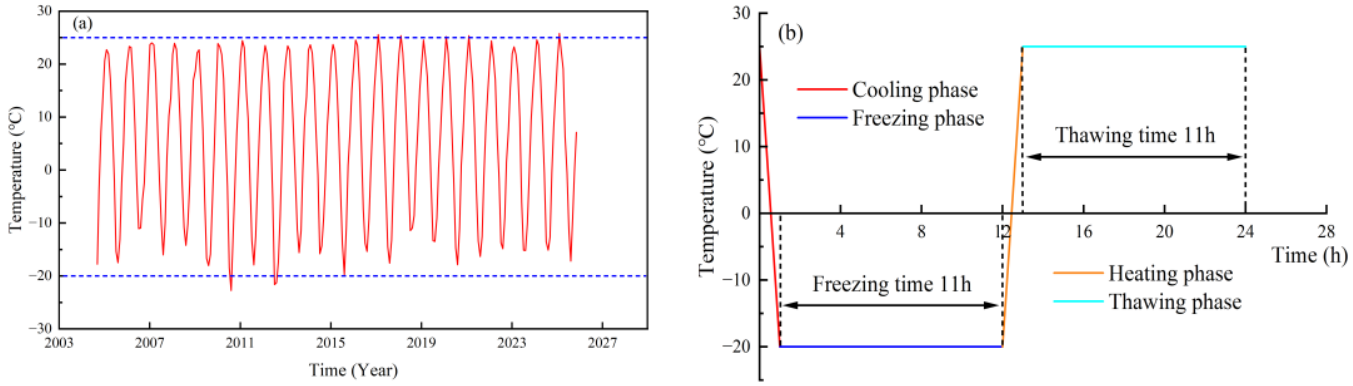


Figure 6. Temperature curve: (**a**) monthly mean temperature in Daqing over the past 20 years; (**b**) temperature control profile for 1 FT cycle.

Previous studies have demonstrated that degradation of soil microstructure and mechanical properties occurs primarily in the early stages of FT cycling and gradually stabilizes after 5–7 cycles [42–44]. Therefore, six FT levels (0, 1, 3, 6, 9, and 12 cycles) were designed in this study. The prepared specimens were labelled as FT0, FT1, FT3, FT6, FT9, and FT12, respectively, where the numerical suffix denotes the total number of FT cycles applied to the specimen. All tests were performed using a fully automatic low-temperature FT testing apparatus (DWR-2, Tianjin, China, Figure 7a). The apparatus has an operating temperature range of −25 to 50 °C with a temperature control accuracy of ±1 °C, enabling reliable simulation of natural temperature variations.

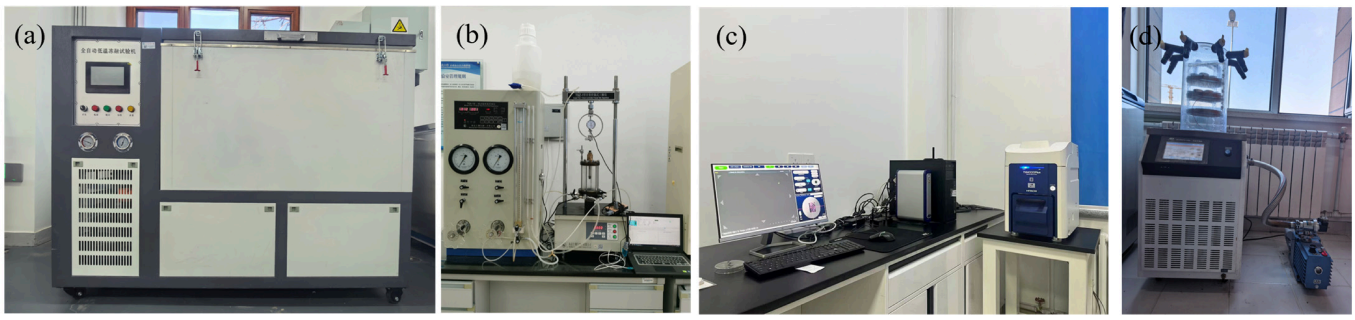


Figure 7. Test instruments: (**a**) fully automatic low-temperature FT testing apparatus; (**b**) TSZ-1 strain-controlled triaxial testing system; (**c**) benchtop SEM; (**d**) vacuum freeze dryer.

2.3.2. Triaxial Compression Test

Following FT treatment, UU triaxial compression tests were performed on the unsaturated specimens using a strain-controlled triaxial system (TSZ-1, Nanjing, China, Figure 7b) in accordance with GB/T 50123-2019 [36]. During testing, confining pressures of 100, 200, and 300 kPa were applied, with the axial loading rate maintained at 0.8 mm/min. Each test was terminated upon reaching an axial strain of 20%.

Three parallel specimens were tested for each combination of FT cycle number and confining pressure. All specimens were prepared and tested under the same conditions following the specified standards and experimental protocols. The replicate results were checked for consistency, and their mean values were used for subsequent analyses.

2.3.3. SEM Tests

The micro-morphology and structural characteristics of dispersive soils subjected to different FT cycles were examined using a TM4000 benchtop scanning electron microscope (Hitachi, Tokyo, Japan; Figure 7c). To preserve the original microstructure induced by FT cycling and to minimize particle skeleton deformation or pore collapse caused by surface tension during conventional drying, all samples were pretreated via vacuum freeze-drying.

Following FT tests, representative soil blocks measuring approximately 10 mm × 10 mm × 5 mm were extracted from the interior of each specimen. The blocks were rapidly frozen in liquid nitrogen and subsequently transferred to a vacuum freeze dryer (SCIENTZ-12N, Ningbo, China; Figure 7d). Drying was conducted for 24 h at −50 °C under a vacuum below 10 Pa, allowing pore ice to sublimate directly. After drying, the samples were cleaved along fresh fracture surfaces to expose flat, undisturbed observation planes, mounted on sample stubs, and coated with a thin gold layer under vacuum to enhance electrical conductivity.

SEM observations were performed in high-vacuum mode with an accelerating voltage of 15 kV and a working distance of 8–12 mm. All images were acquired at a magnification of 1000×, and 3–5 independent fields of view were selected for each group to ensure statistical representativeness. A magnification of 1000× was selected to balance the observation range of soil particle aggregates and the resolution of micropore morphology, which can fully capture the evolution of interparticle contact and pore structure.

The PCAS pore and crack analysis system was used to process the SEM images and extract quantitative parameters, including areal porosity, total pore area, pore count, mean pore area, and pore fractal dimension, to quantify the evolution of soil microstructure under FT cycling.

3. Results and Discussion

3.1. Macroscopic Mechanical Behavior

3.1.1. Stress–Strain Curve

The stress–strain curves of soil specimens subjected to different numbers of FT cycles are presented in Figure 8. All specimens exhibit nonlinear behavior that can be divided into three deformation stages: (i) a linear elastic stage (0–1% axial strain) dominated by interparticle bonding; (ii) a plastic deformation stage (1–5%) with progressively decreasing slope, indicating structural damage and plastic yielding; and (iii) a large-strain stage.

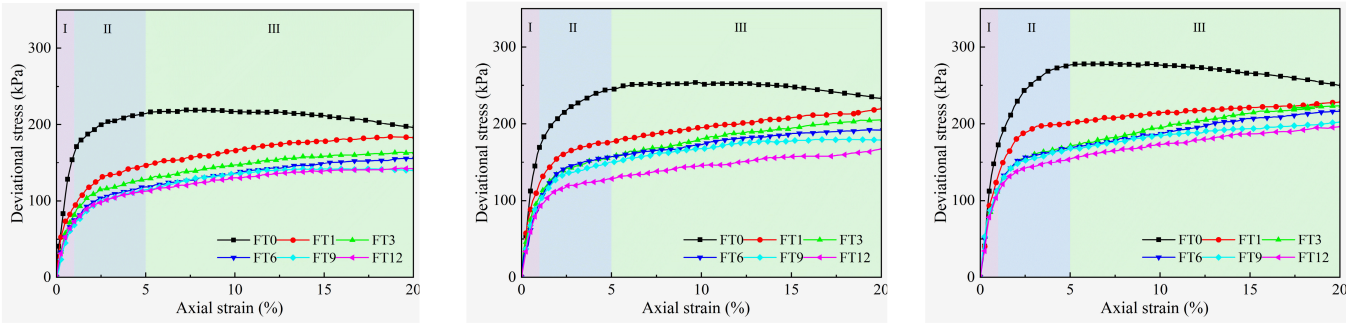


Figure 8. Stress–strain curves of dispersed soil under FT cyclic conditions: (**a**) σ_3 = 100 kPa; (**b**) σ_3 = 200 kPa; (**c**) σ_3 = 300 kPa.

The FT0 specimens reached peak strength at approximately 5% axial strain followed by slight post-peak reduction, indicating weak strain-softening. With increasing FT cycles, the deviatoric stress decreased over the entire strain range, and the response evolved from peak-softening to continuous strain-hardening, consistent with previous studies [45–47],

This transition reflects a weakening of the soil structure: continuous compaction during shearing enhanced interparticle contacts, shifting the dominant strength mechanism from structural bonding to interparticle friction. The differences among FT groups leveled off at large strains, indicating that FT mainly affected strength mobilization during the early and middle stages of loading, without altering the fundamental deformation mechanism.

From a hydrothermal perspective, repeated FT phase transitions induced cyclic volumetric expansion and contraction, rearranging particles, weakening interparticle bonding, and promoting local redistribution of pore water within the evolving pore network. The relatively intact fabric of the untreated specimens enabled rapid stress accumulation and a distinct peak; after FT cycling, freeze-induced structural degradation reduced bonding resistance and increased reliance on friction, accounting for the macroscopic shift from peak-softening to strain-hardening.

A direct shear strain–void ratio relationship would provide an additional state-variable interpretation of this transition. However, the present UU testing system did not record specimen volume change or radial strain during shearing; therefore, a quantitative e–γ relationship cannot be reliably reconstructed from the available data. To avoid introducing unsupported assumptions, the influence of FT-induced structural changes on mechanical behavior is instead interpreted by combining the stress–strain response with the pore-structure evolution quantified by SEM–PCAS in Section 3.2. Direct e–γ measurements could be considered in future work to further establish the quantitative link between structural evolution and shear deformation.

From the perspective of critical-state soil mechanics, this transition can be further interpreted in terms of the relative position of the soil state with respect to the critical-state line. The untreated FT0 specimens, compacted to a relatively low initial void ratio ($e_0 \approx 0.56$, computed from the controlled dry density of 1.68 g/cm^3 and the particle relative density of 2.62) with intact interparticle bonding, lie below the critical-state void ratio at the corresponding mean effective stress; such structured (overconsolidated-like) soils tend to dilate during shearing, mobilizing a peak deviatoric stress followed by strain-softening toward the critical state [48,49]. After FT cycling, although all specimen groups were compacted to the same target density (i.e., the same initial void ratio), frost-induced pore enlargement and coalescence (Section 3.2) substantially damage the interparticle bonding and loosen the soil fabric; the treated specimens therefore behave in a manner similar to normally consolidated (destructured) soils, undergoing continuous compression and strain-hardening without a distinct peak, with the shear resistance governed increasingly by interparticle friction rather than structural bonding [48,50]. This critical-state interpretation, together with the FT-induced pore-structure changes quantified in Section 3.2, provides a mechanistic explanation for the observed transition from strain-softening to strain-hardening behavior.

Confining pressure significantly influences the mechanical behavior. As confining pressure increases from 100 kPa to 300 kPa, both deviatoric stress and initial stiffness increase, and strain-hardening behavior becomes more pronounced. This reflects enhanced lateral confinement and interparticle interlocking, thereby improving shear strength and structural stability [51].

3.1.2. Failure Pattern

The macroscopic failure modes of the triaxial specimens under coupled FT cycling and confining pressure are presented in Figure 9. Across different numbers of FT cycles and confining pressure levels, most specimens maintain an intact cylindrical geometry, with no clearly identifiable shear bands or tensile cracks. During loading, deformation is characterized by uniform lateral expansion, and the specimens ultimately exhibit a typical barrel-shaped bulging response, indicating a globally coordinated ductile deformation mode.

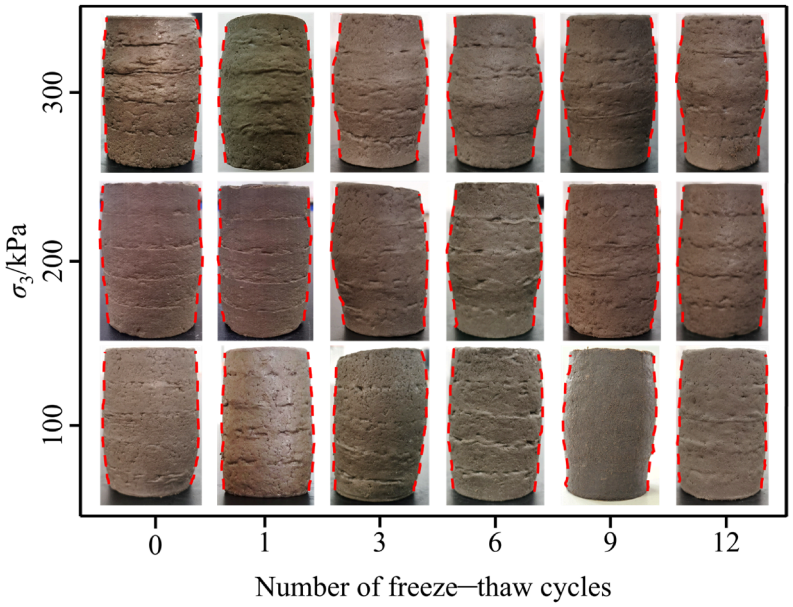


Figure 9. The failure pattern of dispersive soil.

Although no visible shear bands develop in the FT0 specimens, their stress–strain curves still show a distinct peak followed by strain-softening, implying that localized deformation has already initiated at the microstructural level. The distinction between microstructural-level localization and a macroscopic shear band was made on the basis of three combined criteria: (i) visual examination of the post-test specimen surface—no continuous inclined fracture penetrating the full specimen height or diameter was observed macroscopically, mostly uniform lateral bulging; (ii) analysis of the stress–strain response—the post-peak softening was mild (peak-to-residual strength drop typically less than 10% of peak strength) and not accompanied by the abrupt stress drop or dilatancy jump that characteristically accompany shear-band formation; and (iii) the barrel-shaped deformation pattern indicated that strain was distributed across the entire specimen volume rather than concentrated within a narrow localized zone. However, such localization remains spatially scattered and insufficient to evolve into a continuous macroscopic shear failure plane.

With increasing FT cycles, progressive soil structural degradation occurs, accompanied by weakened interparticle cementation and reduced interlocking effects. As a result, strain localization is increasingly inhibited, leading to a more homogeneous deformation pattern. Correspondingly, the stress–strain behavior gradually transitions from strain-softening to strain-hardening with increasing FT cycles.

Overall, FT action induces a transition in the failure mode from localized shear failure to global plastic flow, ultimately manifesting as a typical bulging-type ductile failure.

3.1.3. Evolution of Failure Strength

To quantify strength degradation under FT cycling, different failure criteria were adopted according to the stress–strain response: the deviatoric stress at 15% axial strain was adopted for strain-hardening curves, whereas the peak deviatoric stress was used for strain-softening curves [52–54].

Figure 10a illustrates the evolution of failure strength with FT cycles under confining pressures of 100, 200, and 300 kPa. FT cycling induces pronounced, stage-dependent degradation, with the most significant strength loss occurring within the first three cycles—particularly after the first cycle. Beyond approximately six cycles, the strength tends to stabilize, indicating that degradation approaches a plateau. Quantitatively, at a confining pressure of 100 kPa, the failure strength decreases from 219.11 kPa (FT0) to 178.74 kPa after one cycle

(an 18.42% reduction) and to 158.72 kPa after three cycles (27.56% reduction), eventually leveling off at 139.41 kPa after 12 cycles, representing a cumulative reduction of 36.37%. Similar trends are observed at 200 kPa and 300 kPa, where strengths decline from 253.71 kPa and 278.05 kPa to final values of 157.53 kPa and 186.91 kPa, corresponding to total reductions of 37.91% and 32.78%, respectively (Table 3).

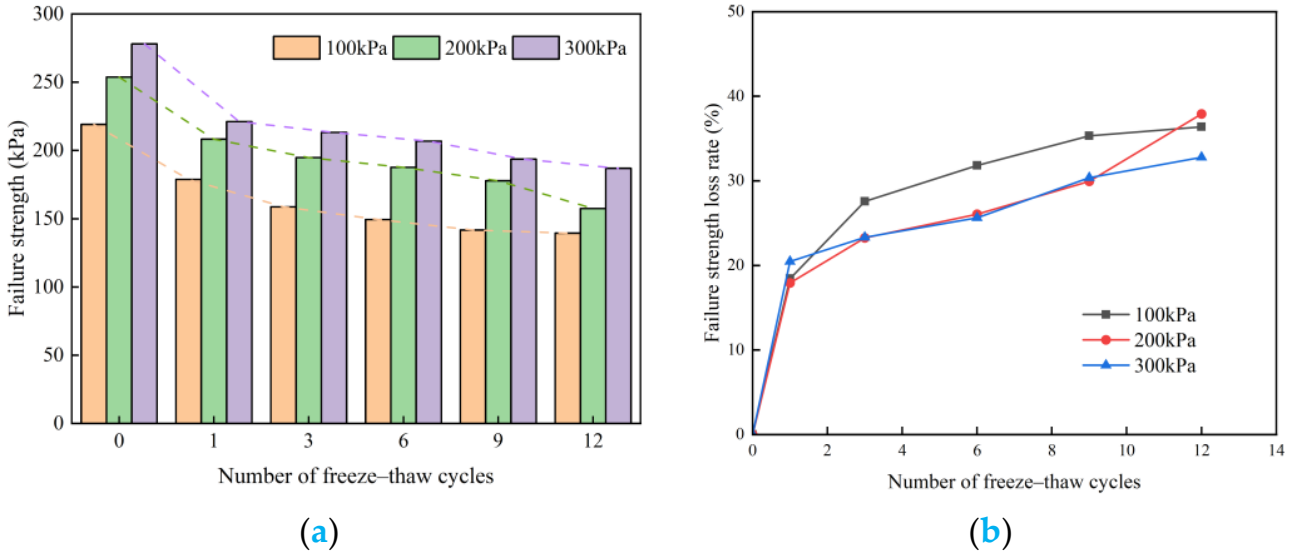


Figure 10. Evolution of failure strength and strength loss ratio of dispersive soil with freeze–thaw cycle number. (**a**) Failure strength under different confining pressures; (**b**) strength loss ratio under different confining pressures.

Table 3. Failure strength and strength loss ratio of dispersive soil under different FT cycles and confining pressure.

FT Cycles	σ_3 = 100 kPa		σ_3 = 200 kPa		σ_3 = 300 kPa	
	Failure Strength (kPa)	Loss Ratio (%)	Failure Strength (kPa)	Loss Ratio (%)	Failure Strength (kPa)	Loss Ratio (%)
0	219.11	0	253.71	0	278.05	0
1	178.74	18.42	208.23	17.93	221.17	20.46
3	158.72	27.56	194.73	23.25	213.21	23.32
6	149.42	31.81	187.62	26.05	206.81	25.62
9	141.74	35.31	177.76	29.94	193.62	30.37
12	139.41	36.37	157.53	37.91	186.91	32.78

Notably, the first freeze–thaw cycle contributes approximately 47–62% of the total strength degradation accumulated over 12 cycles, and the first three cycles jointly account for roughly 60–76% of the overall strength loss. The magnitude of strength degradation per freeze–thaw cycle is highly non-uniform. The incremental strength loss reaches its maximum across the FT0-to-FT1 transition, ranging from 17.93% to 20.46% for the three confining pressures investigated. By contrast, the incremental strength loss between FT6 and FT12 falls to only 0.76–1.98% per cycle, which demonstrates progressive saturation of frost-induced micro-damage within the soil matrix. Thermodynamically, the initial cycles involve the most intensive ice–water phase transitions and associated energy exchange. The resulting freeze-induced volumetric expansion and thermal effects generate internal stresses that disrupt interparticle bonding and the initial soil fabric, leading to increased porosity and loosened particle packing. As cycling continues, the soil structure progressively reorganizes toward a new equilibrium, and damage accumulation gradually saturates, a behavior consistent with previous studies [55–57].

To further characterize this process, the strength loss ratio is defined as

$$\lambda = \frac{Q_0 - Q_N}{Q_0} \times 100\% \quad (1)$$

where Q_0 is the failure strength of the untreated specimen (kPa), and Q_N is the failure strength after N FT cycles (kPa).

Figure 10b shows that the strength loss ratio exhibits a nonlinear evolution, with rapid growth at early stages followed by stabilization at higher cycle numbers. Confining pressure plays a key role in this process. Increasing confining pressure reduces the overall strength loss ratio, indicating that higher confinement suppresses crack propagation and limits pore expansion, thereby enhancing interparticle contact and mitigating structural degradation. The restraining effect of confining pressure on strength degradation can also be explained from the perspective of phase transition thermodynamics. Lateral confining pressure limits the free expansion of pore ice during freezing, increases the internal pressure of the pore system, and reduces the effective volume of pore water involved in the phase transition, thus weakening the structural damage caused by frost heave. At the intermediate confining pressure (200 kPa), a noticeable increase in strength loss is observed at higher cycle numbers, suggesting that cumulative damage becomes dominant after repeated FT disturbance. This reflects a transition from structure-controlled to damage-controlled behavior.

The difference in strength loss ratio between 200 kPa and 300 kPa remains relatively small, indicating reduced sensitivity to confining pressure at higher stress levels. This suggests the existence of a threshold confining pressure beyond which further increases do not proportionally improve resistance to FT-induced degradation. Under such conditions, the restraining effect of confinement on crack growth and pore expansion approaches saturation, and strength degradation is governed primarily by internal structural deterioration.

At the microscale, this strength degradation can be attributed to the coupled effects of frost-driven pore expansion and thaw-induced particle skeleton rearrangement. Ice formation generates internal stresses that promote microcrack initiation and pore enlargement, while thawing leads to particle loosening and partial collapse of the soil skeleton [58]. Repeated FT cycling accelerates irreversible damage accumulation, whereas confining pressure counteracts this process through mechanical restraint. The competition between these mechanisms ultimately governs the evolution of strength degradation.

3.1.4. Evolution of Shear Strength Parameters Under FT Cycles

Shear strength parameters, namely cohesion and internal friction angle, are fundamental indicators for evaluating the shear resistance of soils. In this study, the cohesion and internal friction angle of dispersive soil subjected to FT cycles were determined by constructing Mohr–Coulomb strength envelopes (Figure 11a), and their variations with FT cycle number are presented in Figure 11b.

As shown in Figure 11b, FT cycling exerts an overall deteriorating effect on the shear strength parameters, with cohesion exhibiting a much higher sensitivity than the internal friction angle. Specifically, cohesion shows a pronounced nonlinear decay with increasing FT cycles. The initial cohesion is 84.04 kPa, which decreases to 59.45 kPa after three cycles (a reduction of 29%). Beyond six cycles, the rate of attenuation becomes markedly slower, and cohesion gradually stabilizes at approximately 51.09 kPa, indicating the development of a residual strength state. This behavior suggests that FT-induced damage is most significant during the early stage, while its incremental effect diminishes as structural degradation accumulates.

The underlying mechanism can be attributed to the progressive disruption of soil structure during FT cycling, which represents a coupled HTM process involving pore-water

phase transition, thermally induced stress development, and microstructural evolution. In the initial stage (0–3 cycles), ice lens formation and frost heave during freezing induce substantial stress within the soil matrix, leading to the breakage of interparticle bonding. Upon thawing, meltwater promotes pore generation and weakens particle contacts, and the original bound water gradually transforms into free water and migrates into the expanded pores, resulting in a rapid loss of cohesion. In the sealed, constant-water-content specimens, this cohesion loss is a direct consequence of water phase transitions: on thawing, the water released from pore ice cannot fully return to its original bound state, so the water-mediated bond weakening accumulates with each cycle. With further FT cycles, the soil structure becomes increasingly degraded, and subsequent cycles mainly contribute to the expansion and interconnection of pre-existing pores and microcracks rather than the formation of new structural damage. Consequently, the reduction in cohesion gradually approaches a residual value.

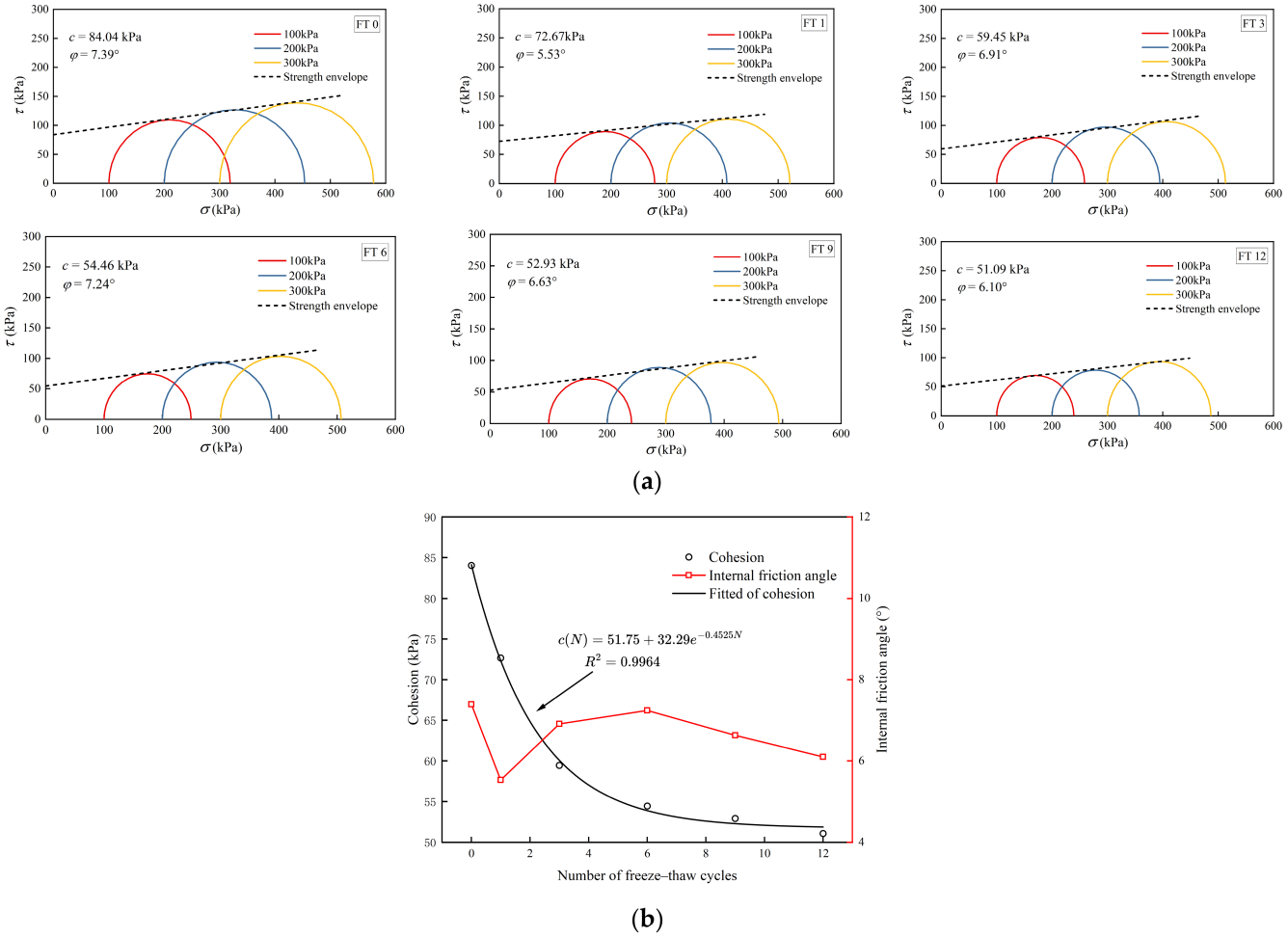


Figure 11. Shear strength parameters of dispersive soil under different freeze–thaw cycles. (**a**) Mohr–Coulomb strength envelopes at various freeze–thaw cycle counts; (**b**) variation of shear strength parameters with freeze–thaw cycle number and exponential fitting of cohesion.

To quantify the experimentally observed attenuation of cohesion, an empirical exponential decay model was proposed in this study. The model is based on the assumption that the rate of cohesion loss is proportional to the remaining cohesion above a residual level, i.e., $dc_N/dN = -b(c_N - c_r)$, where c_N is the cohesion after N FT cycles, c_r is the residual

cohesion, and b is a positive decay coefficient. Integrating this first-order degradation equation with the initial condition $c_N = c_0$ at $N = 0$ gives

$$c_N = c_r + (c_0 - c_r) \times e^{-bN} \quad (2)$$

where c_0 is the initial cohesion (84.04 kPa), c_r is the residual cohesion, and b is the empirical FT degradation coefficient. The model therefore has a clear physical interpretation as a first-order attenuation law toward a residual cohesion state, while N is treated as a cycle-count variable rather than a continuous thermodynamic time variable. The model is not presented as a universal constitutive law; its field of application is limited to the dispersive soil, initial hydraulic state, thermal boundary conditions, and FT range investigated in this study. Fitting gives c_r = 51.75 kPa and b = 0.4525, with R^2 = 0.9964, indicating that the model captures the observed attenuation trend of cohesion under the tested FT conditions.

To facilitate engineering application, Equation (2) can be rewritten in a normalized form to define a cohesion reduction factor $R_c(N)$:

$$R_c(N) = \frac{c_N}{c_0} = (1 - \frac{c_r}{c_0})e^{-bN} + \frac{c_r}{c_0} \quad (3)$$

where $R_c(N)$ is the ratio of the cohesion after N FT cycles to the initial cohesion c_0, and the remaining parameters are identical to those in Equation (2). With the fitted parameters (c_r = 51.75 kPa and b = 0.4525), Equation (3) predicts cohesion reduction factors of 0.86, 0.71, 0.64, 0.62, and 0.62 for N = 1, 3, 6, 9, and 12, respectively, implying that approximately 29% of the initial cohesion is lost within the first three cycles and that the cohesion approaches a residual ratio of approximately 0.62 after about six cycles. A corresponding cohesion degradation index can be defined as $D_c(N) = 1 - R_c(N)$, which increases from 0 to approximately 0.38, providing a quantitative measure of the progressive loss of structural integrity (Table 4).

Table 4. Model-predicted cohesion, cohesion reduction factor $R_c(N)$, and cohesion degradation index $D_c(N)$ of dispersive soil under different FT cycles.

FT Cycles N	c_N (kPa)	$R_c(N) = c_N/c_0$	$D_c(N) = 1 - R_c(N)$
0	84.04	1.000	0
1	72.28	0.860	0.140
3	60.06	0.715	0.285
6	53.89	0.641	0.359
9	52.30	0.622	0.378
12	51.89	0.617	0.383

The proposed reduction factor provides a practical means of estimating the post-FT cohesion of dispersive soil from its initial cohesion, which may facilitate preliminary stability assessments of dispersive soil fills in cold regions where FT-induced degradation needs to be considered.

In contrast, the internal friction angle does not exhibit a clear monotonic trend with increasing FT cycles. Although a slight overall decrease is observed, the variation remains limited, fluctuating within the range of 5.53–7.39°. This difference arises because cohesion is primarily governed by interparticle bonding and soil structure, which are highly susceptible to FT-induced damage, whereas the internal friction angle is mainly controlled by particle friction and geometric arrangement, which are comparatively less sensitive to such environmental effects. The slight fluctuation of internal friction angle is related to the comprehensive effect of pore-water redistribution and particle-arrangement adjustment. On the one hand, the increase of pore space weakens the interlocking effect between parti-

cles, which tends to reduce the friction angle; on the other hand, the particle rearrangement during thaw settlement makes the particle contact more compact, which has a certain enhancement effect on friction. The joint action of the two leads to the non-monotonic fluctuation of internal friction angle.

These macroscopic trends are consistent with the microstructural evolution discussed in the subsequent section. FT cycling leads to a progressive loosening of the soil fabric and the development of a more porous and interconnected structure, which corresponds to the substantial reduction in cohesion. Meanwhile, although the particle contact mode evolves during FT cycling, no obvious changes in particle morphology or surface texture are observed at the SEM scale, suggesting that the intrinsic characteristics of soil particles are largely preserved. This provides a reasonable explanation for the relatively stable yet fluctuating behavior of the internal friction angle.

3.2. Microstructural Evolution

3.2.1. SEM Observations and Degradation Regimes

The microstructural evolution of dispersive soil during FT cycling represents the microscopic response to repeated ice–water phase transitions and associated pore-water redistribution induced by thermal cycling. These coupled HTM processes govern the progressive adjustment of soil fabric, resulting in three distinct degradation regimes with different dominant mechanisms (Figure 12).

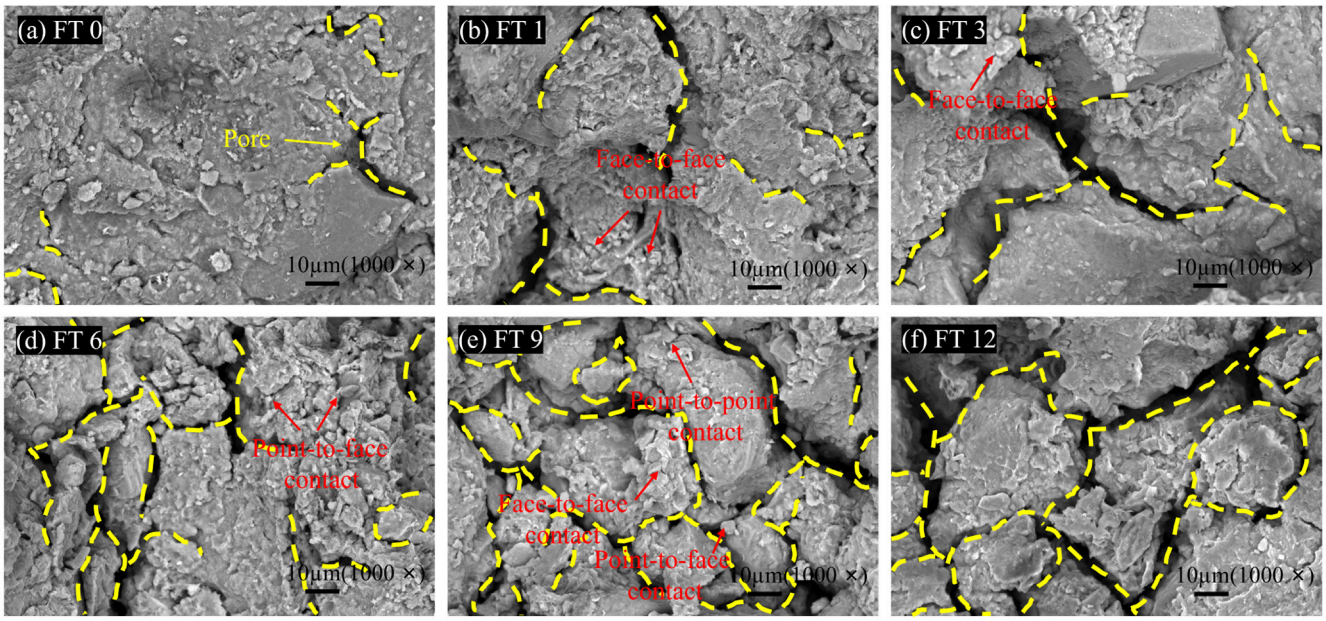


Figure 12. SEM micrographs of soil specimens subjected to various freeze–thaw cycles (1000×).

In the initial stage (FT0–FT1), the in situ freezing of pore water generates freeze-induced expansion stress, which preferentially affects weak interparticle bonding regions and pore boundaries. This process initiates localized degradation of interparticle bonding and pore enlargement while largely preserving the overall integrity of the soil skeleton. Consequently, the soil structure gradually evolves from a dense, well-connected fabric toward a transitional framework characterized by enlarged but relatively isolated pores, while face-to-face particle contacts remain dominant.

With increasing FT cycles (FT3–FT6), repeated phase transitions drive continuous accumulation of frost heave energy and gradual redistribution of pore water toward larger voids under temperature gradients and crystallization pressure. This process progressively weakens interparticle cementation and triggers a connectivity-controlled degradation

regime: residual pore expansion accumulates, pore boundaries become irregular, and pore connectivity improves significantly, as evidenced by a progressive increase in the number of pore throats visible in SEM micrographs, the coalescence of previously isolated micropores into elongated or branched pore clusters, and the concomitant decrease in pore count together with an increase in mean pore area quantified by PCAS (see Section 3.2.3). The evolution of pore connectivity was therefore assessed not by qualitative observation alone but by combining visual inspection of pore network morphology with quantitative PCAS-derived parameters—specifically the concurrent decrease in pore count and increase in mean pore area, which are widely accepted as indirect indicators of pore coalescence and enhanced interconnection. It should be acknowledged that a fully quantitative 3D assessment of connectivity would require X-ray micro-computed tomography (μCT) or mercury intrusion porosimetry (MIP), and this limitation is further discussed in Section 5. Pore connectivity improves significantly, and the dominant particle contact mode evolves from face-to-face to point-to-face, indicating the initiation of structural disassembly and localized particle rearrangement.

In the later stage (FT9–FT12), microscale redistribution of pore water occurs within the progressively altered pore network, and FT-induced phase transition becomes increasingly associated with larger and more connected pores; the soil enters a particle-interlock friction-dominated regime. Cementation is largely destroyed, and the soil fabric transforms into a highly porous, interconnected granular assembly. Pore coarsening and coalescence lead to the development of a connected fissure-like network, while interparticle contacts evolve toward point-to-point dominance. The mechanical behavior is thus governed by frictional sliding rather than structural bonding.

Overall, FT cycling induces a fundamental regime transition from a cementation-dominated structure to a connectivity-controlled degradation state, and ultimately to a friction-dominated granular system.

The observed regime transitions can be interpreted within established theoretical frameworks. From the viewpoint of structured-soil mechanics, the progressive loss of strength reflects the competition between interparticle bonding and ice crystallization pressure: when the local crystallization pressure exceeds the bond strength, bonds rupture preferentially along weak contacts, analogous to the bond-breakage mechanism underlying the structural yield of cemented clays. Thermodynamically, the coexistence of pore ice and unfrozen water is governed by the generalized Clausius–Clapeyron relation, which predicts that pore water migrates toward larger pores driven by the curvature-dependent equilibrium temperature [20,59,60]; this provides a quantitative basis for the observed transition from a micropore-dominated fabric toward a macropore-connected structure. However, the high ESP and the weakly cemented flocculated fabric of dispersive clay make its initial bonding more vulnerable, so the transition occurs more rapidly, and the cohesion loss is more pronounced than in non-dispersive soils [61]. Because the specimens were sealed and their water content stayed essentially constant, the progressive transfer of pore water toward larger pores must occur at the expense of water films in smaller pores, implying that the fabric change is an internal, water-driven reorganization.

3.2.2. Areal Porosity and Total Pore Area

The variations in areal porosity and total pore area with increasing FT cycles are shown in Figure 13. Both parameters exhibit a continuous increase, indicating progressive microstructural degradation.

The untreated specimen exhibits a total pore area of 786.83 μm^2 and an areal porosity of 6.98%. After 12 FT cycles, these values increase to 2886.42 μm^2 and 25.61%, corresponding

to overall growths of 266.8% and 266.9%, respectively. The nearly identical evolution of both indices confirms that pore area expansion is the primary control on porosity development.

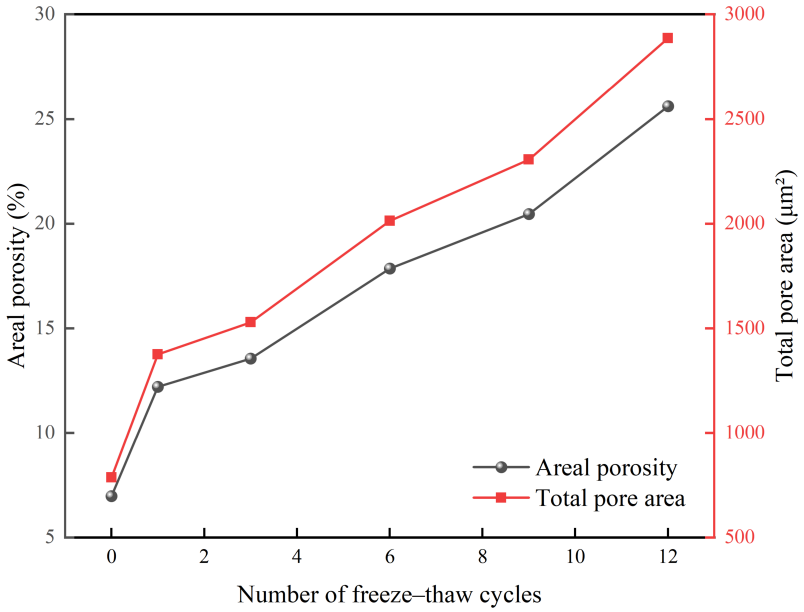


Figure 13. Variations in areal porosity and total pore area with increasing FT cycles.

Although the volumetric expansion of pure water during freezing is approximately 9%, the substantially larger increase in areal porosity demonstrates that the observed pore evolution cannot be explained solely by primary phase-change expansion. Instead, repeated FT cycling promotes cumulative structural rearrangement, pore enlargement, and pore coalescence, resulting in progressive modification of the soil pore architecture. Each FT cycle contributes to partially irreversible pore structure alteration, leading to long-term evolution of the pore network. This cumulative, partially irreversible character of pore evolution is consistent with pore-scale observations in other fine-grained soils [32,59]. As the specimen water content remained essentially constant throughout cycling, this growth cannot be explained by external water ingress and instead reflects internal pore-water redistribution accompanied by phase-change-induced structural rearrangement.

A pronounced stage-dependent response is observed. The first FT cycle induces a 74.9% increase in both parameters, accounting for 28.10% of the total 12-cycle evolution, highlighting the dominant role of the initial freezing event. Subsequent cycles (FT3–FT12) are characterized by steady but moderate growth (10–20% per cycle), without signs of saturation or reversal.

This evolution is governed by a transition in the degradation mechanism. In the initial stage, FT action primarily activates pre-existing micropores and interparticle defects, leading to rapid structural dilation. With continued cycling, the mechanism shifts toward progressive pore enlargement, accompanied by an expanding influence zone of frost heave stresses, which promotes continuous pore coarsening and connectivity development.

Overall, FT cycling drives a cumulative and irreversible enlargement of the pore system, controlled by an initial defect-activation regime followed by sustained stress-driven pore expansion.

3.2.3. Pore Count and Mean Pore Area

The variations in mean pore area and pore count are presented in Figure 14. In contrast to the monotonic increase in porosity, these two parameters exhibit a clear inverse trend, reflecting FT-induced pore coalescence and the development of larger pores.

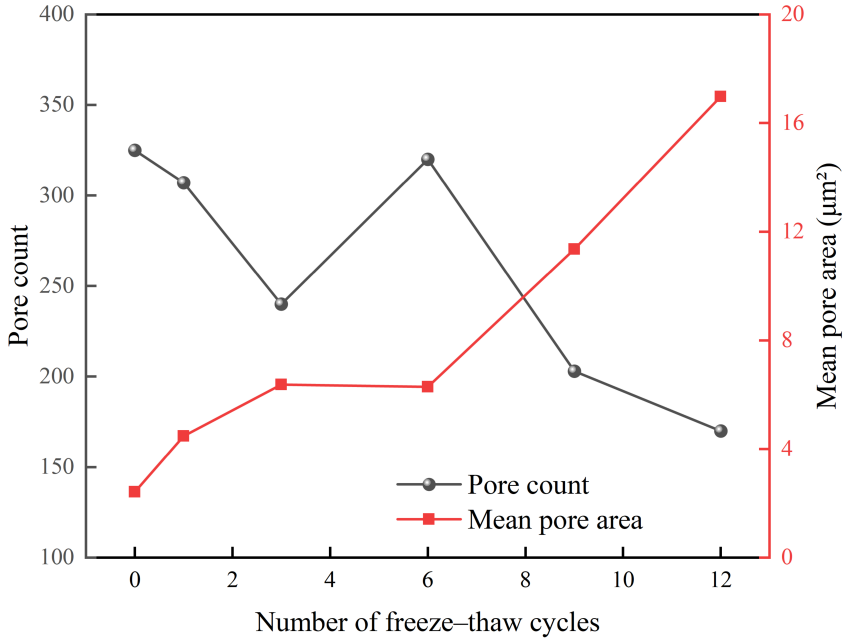


Figure 14. Variations in pore count and mean pore area with increasing FT cycles.

For the untreated specimen, the pore count is 325 with a mean pore area of 2.42 μm^2. With increasing FT cycles, pore count generally decreases while mean pore area increases. After 12 cycles, these values reach 170 (−47.7%) and 16.98 μm^2 (+601.3%), respectively.

The evolution is not strictly monotonic. After three cycles, pore count decreases to 240 and mean pore area rises to 6.37 μm^2. After six cycles, pore count temporarily increases to 320, while mean pore area remains nearly unchanged (6.37→6.29 μm^2). This inverse relationship is governed by frost heave-induced pore coalescence. Repeated FT cycling promotes expansion of micropores and thinning of inter-pore walls; once the local stress exceeds matrix strength, pore walls rupture, and adjacent pores merge, reducing pore count while increasing pore size.

The non-monotonic response reflects competition between pore coalescence and pore nucleation. In the early stage (≤FT3), coalescence dominates, leading to decreasing pore count and rapid growth in mean pore area. At six FT cycles, secondary micropores nucleate along interfaces and defects, temporarily increasing pore count. With further cycling, coalescence again dominates, resulting in renewed pore merging and continued growth of mean pore area.

Overall, FT cycling induces a nonlinear but directionally consistent pore evolution characterized by alternating dominance between pore coalescence and pore nucleation. Comparable competition between pore coalescence and secondary pore nucleation has been reported in MIP- and NMR-based studies of FT-affected soils [23,32].

3.2.4. Pore Fractal Dimension

Fractal dimension is a fundamental parameter for quantifying the self-similarity and interfacial complexity of pore structures in porous media. It provides a refined perspective on how FT cycles reshape the soil microstructure. As shown in Figure 15, the pore boundary fractal dimension of the specimens remains within a narrow range of 1.2549 to 1.2686. With increasing FT cycles, it exhibits a generally decreasing trend with local fluctuations. The initial fractal dimension of the untreated specimen is 1.2614, and no significant order-of-magnitude change is observed after FT cycling. After 12 FT cycles, it decreases to 1.2549, corresponding to an overall reduction of 0.52%, indicating that FT action does not fundamentally alter the complexity of the pore structure.

From a thermo-mechanical perspective, the evolution of fractal dimension can be attributed to the progressive adjustment of pore geometry under repeated ice–water phase transitions. Freeze-induced localized stresses promote pore restructuring, while subsequent pore coalescence reduces boundary tortuosity and geometric complexity. Microscopically, this process is manifested as the gradual merging of adjacent micropores as thin matrix partitions are disrupted during repeated freezing–thawing cycles. The initial specimen contains numerous primary micropores with fragmented boundaries and pronounced local asperities, resulting in relatively high interfacial complexity. With continued FT cycling, pore enlargement and coalescence progressively smooth irregular boundary features, leading to reduced interfacial complexity and a decrease in fractal dimension. This evolution indicates that FT-induced degradation is primarily controlled by changes in pore size and connectivity rather than by increased boundary irregularity.

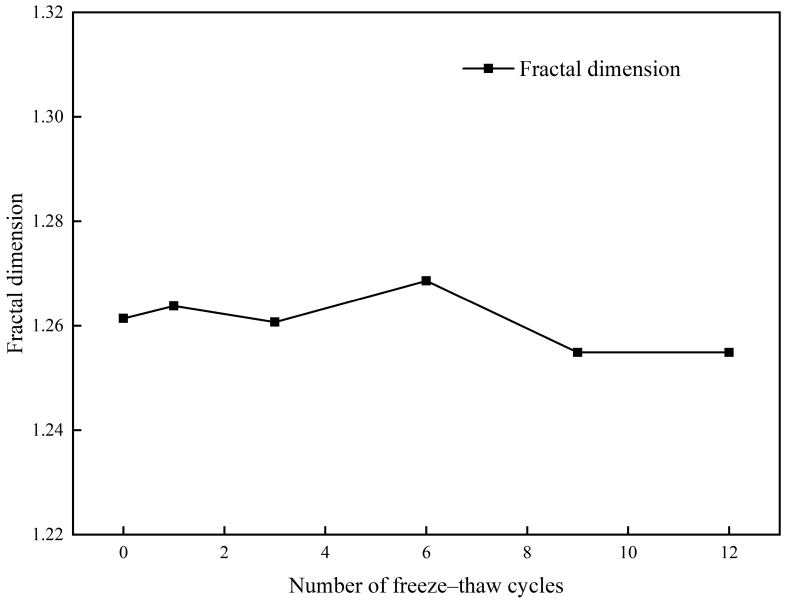


Figure 15. Variation of fractal dimension with increasing FT cycles.

The local fluctuations in fractal dimension correspond to the dynamic competition between pore nucleation and pore coalescence. At the sixth FT cycle, a temporary increase in fractal dimension is observed, consistent with intensive nucleation of secondary micropores within the soil matrix. As frost heave stress accumulates, numerous secondary pores form along particle interfaces and pre-existing micro-defects. These newly formed pores possess more irregular and fragmented boundaries, temporarily increasing interfacial complexity. In subsequent cycles, pore coalescence again becomes dominant. Newly generated micropores progressively expand and merge, and the boundary irregularities are progressively reduced, leading to a resumption of the overall decreasing trend.

Overall, the evolution of fractal dimension confirms the microstructural degradation mechanism from the perspective of structural complexity. The primary effect of FT action is to promote pore expansion, interconnection, and coalescence, resulting in substantial growth in pore size, while exerting limited influence on pore boundary complexity and self-similarity. The narrow variation range and weak downward trend further indicate that microstructural degradation is mainly associated with quantitative changes in pore size rather than qualitative transformation of pore morphology. These findings provide a fractal-based quantitative framework for characterizing the stage-dependent evolution of FT-induced damage.

3.3. HTM Coupling Mechanism of FT-Induced Degradation

Combining the macroscopic mechanical responses and microscopic pore structure evolution, a HTM coupling mechanism is proposed to explain the degradation of dispersive soil subjected to FT cycling.

(1) Hydro-thermal phase-transition driving stage: Under cyclic ambient temperature fluctuations, heat transfer induces repeated ice–water phase transitions within pore spaces. This process involves latent heat exchange and approximately 9% volumetric expansion during freezing, generating freeze-induced stresses inside the soil matrix. Such phase-transition-induced stresses provide the primary driving force for structural adjustment and mechanical degradation during FT cycling. At this stage, pore water acts as the primary driver of structural deterioration. The cryogenic migration of unfrozen film water, triggered by interface cryosuction toward the freezing front and larger voids, directly concentrates frost-heave/phase-change stresses on pore walls and drives continuous microstructural reorganization within the pore network.
(2) Pore structure evolution stage: Freeze-induced stresses preferentially affect interparticle bonding regions and pre-existing defects, causing weakening of particle connections and promoting micropore expansion, coalescence, and connectivity development. With increasing FT cycles, the pore system gradually evolves from a dense structure dominated by small isolated pores toward a looser structure characterized by enlarged and interconnected pores. Meanwhile, the pore-water redistribution may occur within the evolving pore network.
(3) Macroscopic mechanical response stage: The weakening of interparticle bonding and progressive pore structure degradation jointly reduce soil cohesion, leading to a gradual transition of the dominant strength mechanism from structural bonding to frictional resistance. These microstructural changes are manifested macroscopically as a transition from strain-softening to strain-hardening behavior, a shift from localized shear concentration to overall plastic deformation with barrel-shaped bulging, and a staged strength degradation pattern characterized by rapid early-stage reduction followed by gradual stabilization.

3.4. Comparative Analysis with Other Soil Types

To assess the generality of the observed degradation behavior, the results of this study are compared with published data for other soil types subjected to FT cycling (Table 5). Despite differences in soil type, testing conditions, and cycle numbers, a common degradation pattern emerges: (i) shear strength and cohesion decrease most rapidly during the initial 1–3 cycles and stabilize after approximately 5–7 cycles [26,27,43]; (ii) the internal friction angle is only slightly affected, exhibiting either a minor decrease or non-monotonic fluctuations [24,26]; and (iii) degradation is invariably accompanied by pore enlargement, increased connectivity, and progressive weakening of interparticle bonding [23,32,58].

Nevertheless, the degradation magnitude, rate, and underlying dominant mechanisms remain soil-specific [26,35,45,51]. For the dispersive soil investigated here, the mechanical response shifted progressively toward friction-dominated behavior during cycling. This pronounced degradation is primarily attributed to high ESP and weak interparticle bonding, which facilitate particle rearrangement and pore expansion during repeated ice–water phase transitions. Overall, while the stage-dependent degradation observed in this study is broadly consistent with general fine-grained soil behavior, the relative contributions of cohesion and friction vary with soil fabric, mineralogy, and initial hydraulic states. Further comparative studies across soils with varying dispersivity levels and mineral compositions are required to evaluate the quantitative generality of the proposed mechanism.

Table 5. Qualitative comparison of FT-induced degradation behavior reported for different soil types (synthesized from the cited references).

Soil Type	Test Method	Reported FT Degradation Trend	Reference
Dispersive clay (this study)	UU triaxial; SEM/PCAS	Cohesion decays exponentially (−29% after 3 cycles; about −38% at stabilization); phi fluctuates within 5.53–7.39 deg	This study
Qinghai–Tibet clay	Triaxial tests	Cohesion decreases continuously; phi slightly increases	[24]
Recompacted loess	True triaxial tests	Cohesion decreases and stabilizes; phi less sensitive	[26]
Frozen loess	Uniaxial/triaxial	Strength decreases mainly in early cycles	[43]
Silt	Deformation and microstructure	Strength decreases; pore structure loosens	[58]
Silty clay (dry–wet–FT coupled)	Shear tests	Strength decreases and stabilizes with cycling	[27]
Geogrid-reinforced expansive soil	Shear tests	Progressive strength loss under FT	[28]

3.5. Water-Related Engineering Implications

This study originates from the hydraulic engineering context of the South Nenjiang Main Canal and directly addresses water-related degradation processes central to the safety of water conservancy infrastructure in seasonally frozen regions. Because the sealed specimens neither gained nor lost water, the degradation of pore structure and shear strength is driven entirely by in situ phase changes and the internal movement of pore water. This water-process-based degradation chain (soil-water phase transition → pore-water redistribution → pore expansion and coalescence → cohesion loss) can be incorporated into stability assessments of canal embankments and earth dams, while the proposed cohesion reduction factor and degradation index provide practical tools for slope-stability and seepage-related safety evaluations. These results also provide a controlled baseline for distinguishing intrinsic water-phase-change effects from open-system water-supply effects, which is essential for interpreting field observations of frost heave, thaw settlement, and seepage-induced erosion.

4. Conclusions

This study investigates dispersive soil sampled from the South Nenjiang Main Canal in Heilongjiang Province. A series of UU triaxial compression tests were conducted under different FT cycles. Combined with SEM- and PCAS-based quantitative image analysis, the evolution of mechanical behavior and the associated microstructural degradation mechanisms were systematically examined. The principal novelty of this work is the establishment of an explicit micro–macro degradation chain for dispersive clay under FT cycling—ice–water phase transitions, pore expansion and coalescence, interparticle bond breakage, and the transition from structure-controlled to friction-dominated strength—together with a quantitative cohesion reduction model and a degradation index. The main conclusions are as follows:

(1) Transition in Stress–Strain and Failure Modes: FT cycling alters the stress–strain behavior from mild strain-softening with distinct peak strength (untreated) to continuous strain-hardening (post-FT). Macroscopically, all specimens exhibit ductile barrel-shaped bulging failure without through-going shear bands, reflecting a shift from localized micro-shear failure to global plastic deformation.

(2) Stage-Dependent Strength and Cohesion Degradation: Failure strength degradation is highly stage-dependent: the first three FT cycles account for 60–76% of total strength loss, beyond which degradation stabilizes after approximately six cycles. Cohesion exhibits severe exponential attenuation from 84.04 kPa to a residual value of ~51 kPa (residual ratio ~0.62), whereas the internal friction angle remains largely stable (5.53–7.39°), demonstrating that cohesion loss dominates the strength deterioration.

(3) Microstructural Evolution: Repeated FT cycling promotes progressive pore coarsening, increasing areal porosity by over 260% and shifting particle contacts from face-to-face to point-to-point, which underpins the strength degradation described above.

(4) A normalized cohesion reduction factor (Equation (3)) and a cohesion degradation index were proposed to quantify the progressive loss of structural integrity, providing a simple design-oriented tool for estimating the long-term cohesion of dispersive soils in cold regions and for preliminary stability assessment of canal and embankment structures.

(5) The closed-system experiments with an essentially constant total water content demonstrate that FT-induced degradation of dispersive soil is fundamentally a water-phase-transition-driven process, in which the phase change and redistribution of the initially available pore water control the evolution of pore structure and shear strength. These findings provide a water-process-based basis for the stability assessment of hydraulic infrastructure in seasonally frozen regions.

The findings of this study provide experimental evidence for the design and long-term performance evaluation of dispersive soil engineering structures such as canals and embankments in seasonally frozen regions. Future research should further investigate the regulatory effects of water content and soil improvement measures on FT-induced degradation, so as to improve the theoretical framework for stability assessment of dispersive soils in cold-region engineering.

5. Limitations and Future Work

Although previous studies have systematically characterized the mechanical degradation and microstructural evolution of dispersive soils under FT cycles, several limitations remain. First, most experiments were conducted under closed, constant-moisture conditions, neglecting groundwater-driven moisture migration and solute redistribution, thereby limiting the realistic representation of in situ hydro–thermal coupling processes. These processes have been widely shown to significantly influence pore structure evolution and mechanical properties during FT cycles [32,62]. Second, the UU triaxial tests capture only instantaneous mechanical responses and cannot reflect time-dependent processes such as creep, which are critical for evaluating the long-term stability of soils subjected to FT cycles [63]. Third, the absence of frost heave and volumetric strain measurements precludes direct quantification of the linkage between ice–water phase transition-induced expansion and structural damage; in particular, the initial-cycle frost heave strain, critical for validating the observed porosity increase and exponential cohesion decay, remains unresolved [21,24,64]. Fourth, mineralogical and elemental changes were not directly characterized; complementary X-ray diffraction (XRD) and energy-dispersive X-ray spectroscopy (EDX/EDS) analyses are recommended to link mineral composition to FT-induced structural degradation and to strengthen the SEM-based interpretation. Fifth, the freezing rate was fixed to a single programmed profile and was not treated as an independent variable; because the freezing rate controls pore-ice crystal size and morphology [59], rate-dependent experiments are needed to isolate its contribution to structural damage. Sixth, although the cycle design (0, 1, 3, 6, 9, and 12) concentrated resolution on the early stage and successfully captured the dominant degradation, additional intermediate cycles

(e.g., 2, 4, and 5) would further refine the resolution of the degradation process within the first three cycles. Seventh, only one dispersive soil type was tested; comparative tests on soils with different clay mineralogy and dispersivity are required to validate the universality of the proposed model and degradation index. Finally, a robust quantitative framework linking microstructural evolution to macroscopic constitutive behavior under multi-field coupling conditions has yet to be established.

Future work should prioritize: (i) developing open-system experimental frameworks incorporating HTM coupling to better reproduce field conditions; (ii) conducting long-term mechanical tests, such as creep experiments, to characterize time-dependent deformation behavior and improve stability assessments under FT conditions; (iii) establishing constitutive models incorporating FT-induced damage accumulation to bridge micro–macro behavior and enable predictive simulations; and (iv) implementing real-time monitoring of frost heave and volumetric deformation to quantify the relationships among phase transition, structural evolution, and strength degradation. Future work should also perform XRD and EDX/EDS analyses to complement the SEM observations, and explore the effects of freezing rate and open-system water supply on the degradation behavior.

Addressing these challenges is essential for advancing predictive understanding of soil behavior under coupled environmental loading and for improving the reliability of long-term stability assessment and design in cold-region geotechnical systems.

Author Contributions: Conceptualization, X.L. and E.W.; methodology, X.L.; formal analysis, X.L.; investigation, X.L., X.Z., J.S. and Y.Z.; resources, E.W.; data curation, X.L.; writing—original draft preparation, X.L.; writing—review and editing, E.W., H.J. and H.H.; project administration, R.G., Q.L. and L.W.; funding acquisition, E.W. and L.W. All authors have read and agreed to the published version of the manuscript.

Funding: This work was supported by the research project of the major water conservancy project for enhancing grain production capacity in Heilongjiang Province (Grant No. WSLJ-JSFW-2025-04) and the Science and Technology Plan of Xinjiang Production and Construction Corps (Grant No. 2024AB09).

Data Availability Statement: The original contributions presented in this study are included in the article. Further inquiries can be directed to the corresponding author.

Acknowledgments: In the preparation of this manuscript, ChatGPT-5.6 Luna, Doubao and Kimi K2.6 were used to assist with language polishing and text readability optimization. All AI-assisted content has been carefully reviewed, edited and validated by the authors, who bear full responsibility for the whole manuscript, including all data, interpretations and conclusions.

Conflicts of Interest: Authors Renhui Guan, Qixun Lv, and Liqiang Wang were employed by the company Heilongjiang Provincial River Regulation Engineering Construction Management Co., Ltd. The remaining authors declare that the research was conducted in the absence of any commercial or financial relationships that could be construed as a potential conflict of interest.

References

1. Rengasamy, P.; Tavakkoli, E.; McDonald, G.K. Exchangeable cations and clay dispersion: Net dispersive charge, a new concept for dispersive soil. *Eur. J. Soil Sci.* **2016**, *67*, 659–665. [CrossRef]
2. Sherard, J.L.; Dunnigan, L.P.; Decker, R.S. Identification and nature of dispersive soils. *J. Geotech. Eng. Div.* **1976**, *102*, 287–301. [CrossRef]
3. Bell, F.G.; Maud, R.R. Dispersive soils: A review from a South African perspective. *Q. J. Eng. Geol.* **1994**, *27*, 195–210. [CrossRef]
4. Vyas, S.; Anand, B.; Kumar, R.; Gupta, S.L. Characterization of Dispersive Soils. *Lect. Notes Civ. Eng.* **2022**, *167*, 421–428. [CrossRef]
5. Zhang, X.; Liu, Z.; Han, Y. Progress towards the identification and improvement of dispersive soils: A review. *Eur. J. Soil Sci.* **2024**, *75*, e70002. [CrossRef]
6. Page, K.L.; Dang, Y.P.; Dalal, R.C.; Kopittke, P.M.; Menzies, N.W. The impact, identification and management of dispersive soils in rainfed cropping systems. *Eur. J. Soil Sci.* **2021**, *72*, 1655–1674. [CrossRef]

7. Vakili, A.H.; Salimi, M.; Keskin, İ.; Jamalimoghadam, M. A systematic review of strategies for identifying and stabilizing dispersive clay soils for sustainable infrastructure. *Soil Tillage Res.* **2024**, *239*, 106036. [CrossRef]
8. Shi, Z.; Chen, H.E.; Yuan, X.; Zhang, Y.; Zhang, X. Laboratory tests for comprehensive determination method of soil dispersion grades. *J. Eng. Geol.* **2020**, *28*, 482–489. (In Chinese) [CrossRef]
9. Rengasamy, P.; Marchuk, A. Cation ratio of soil structural stability (CROSS). *Soil Res.* **2011**, *49*, 280–285. [CrossRef]
10. Ouhadi, V.R.; Goodarzi, A.R. Assessment of the stability of a dispersive soil treated by alum. *Eng. Geol.* **2006**, *85*, 91–101. [CrossRef]
11. Mohanty, S.; Roy, N.; Singh, S.P.; Sihag, P. Estimating the Strength of Stabilized Dispersive Soil with Cement Clinker and Fly Ash. *Geotech. Geol. Eng.* **2019**, *37*, 2915–2926. [CrossRef]
12. He, J.; Gao, P.; Yang, H.; Tian, W.; Ding, J. Triaxial testing and model study on lime modified dispersive soil considering age effects. *Bull. Eng. Geol. Environ.* **2024**, *83*, 456. [CrossRef]
13. Goodarzi, A.R.; Salimi, M. Stabilization treatment of a dispersive clayey soil using granulated blast furnace slag and basic oxygen furnace slag. *Appl. Clay Sci.* **2015**, *108*, 61–69. [CrossRef]
14. Zhao, G.; Zhu, Z.; Ren, G.; Wu, T.; Ju, P.; Ding, S.; Shi, M.; Fan, H. Utilization of recycled concrete powder in modification of the dispersive soil: A potential way to improve the engineering properties. *Constr. Build. Mater.* **2023**, *389*, 131626. [CrossRef]
15. Türköz, M.; Umu, S.U.; Öztürk, O. Effect of Silica Fume as a Waste Material for Sustainable Environment on the Stabilization and Dynamic Behavior of Dispersive Soil. *Sustainability* **2021**, *13*, 4321. [CrossRef]
16. Wang, E.; Li, Y.; Ren, Z.; Jiang, H.; Liu, C.; Zou, Y.; Du, S. Microstructural change of improved dispersive soil based on scanning electron microscope and nuclear magnetic resonance technology. *Chin. J. Geotech. Eng.* **2023**, *45*, 1123–1132. (In Chinese) [CrossRef]
17. Reddy, J.J.; Varaprasad, B.J.S. Long-term and durability properties of xanthan gum treated dispersive soils—An eco-friendly material. *Mater. Today Proc.* **2021**, *44*, 309–314. [CrossRef]
18. Abbasi, N.; Farjad, A.; Sepehri, S. The Use of Nanoclay Particles for Stabilization of Dispersive Clayey Soils. *Geotech. Geol. Eng.* **2017**, *36*, 327–335. [CrossRef]
19. Vakili, A.H.; Shojaei, S.I.; Salimi, M.; Selamat, M.R.B.; Farhadi, M.S. Contact erosional behaviour of foundation of pavement embankment constructed with nanosilica-treated dispersive soils. *Soils Found.* **2020**, *60*, 167–178. [CrossRef]
20. Li, S.; Zhang, M.; Pei, W.; Lai, Y. Experimental and numerical simulations on heat-water-mechanics interaction mechanism in a freezing soil. *Appl. Therm. Eng.* **2018**, *132*, 209–220. [CrossRef]
21. Qi, J.; Vermeer, P.A.; Cheng, G. A review of the influence of freeze-thaw cycles on soil geotechnical properties. *Permafr. Periglac. Processes* **2006**, *17*, 245–252. [CrossRef]
22. Bai, Y.; Liu, X.; Dang, Y.; Duan, T.; He, Y. Mechanical Properties and Degradation Mechanisms of Shallow Ili Loess Under Freezing and Thawing Conditions. *Appl. Sci.* **2025**, *15*, 12658. [CrossRef]
23. Zhu, H.; Sun, S.; Yang, X.; Chen, K.; Ding, Z. Coupling Mechanisms Among Water Content, Pore Characteristics, and Permeability in Northeast China's Black Soils During Freeze–Thaw Cycles. *Agriculture* **2026**, *16*, 1066. [CrossRef]
24. Wang, D.; Ma, W.; Niu, Y.; Chang, X.; Wen, Z. Effects of cyclic freezing and thawing on mechanical properties of Qinghai–Tibet clay. *Cold Reg. Sci. Technol.* **2007**, *48*, 34–43. [CrossRef]
25. Yang, Z.; Mou, X.; Ji, H.; Liang, Z.; Zhang, J. Effects of freeze-thaw on bank soil mechanical properties and bank stability. *Sci. Rep.* **2024**, *14*, 9808. [CrossRef] [PubMed]
26. Zheng, F.; Shao, S.; Wang, S. Effect of freeze-thaw cycles on the strength behaviour of recompacted loess in true triaxial tests. *Cold Reg. Sci. Technol.* **2021**, *181*, 103172. [CrossRef]
27. Guo, H.; Sun, Y.; Sun, C.; Gu, H. Experimental study on shear strength and deterioration behavior of silty clay under dry-wet-freeze-thaw cycles. *Sci. Rep.* **2025**, *15*, 17907. [CrossRef] [PubMed]
28. Yang, Z.; Liu, J.; Zhang, R.; Shi, W.; Yuan, S. Shear Resistance Evolution of Geogrid Reinforced Expansive Soil Under Freeze–Thaw Cycles. *Appl. Sci.* **2025**, *15*, 5492. [CrossRef]
29. Han, Y.; Wang, Q.; Xia, W.; Liu, J.; Wang, J.; Chen, Y.; Shen, J. Experimental study on the hydraulic conductivity of unsaturated dispersive soil with different salinities subjected to freeze-thaw. *J. Hydrol.* **2019**, *583*, 124297. [CrossRef]
30. Zhang, S.; Xu, X.; Dong, X.; Lei, H.; Sun, X. Effects of Freeze–Thaw Cycles on the Mechanical Properties and Microstructure of a Dispersed Soil. *Appl. Sci.* **2023**, *13*, 9849. [CrossRef]
31. Zhang, Y.; Han, C. Mechanical Properties and Microstructure of Dispersed Soils underDifferent Freeze-thaw Cycles. *For. Eng.* **2024**, *40*, 204–211. (In Chinese)
32. Fan, W.; Yang, P.; Wang, S.; Zuo, X.; Chen, Y. Multiscale analysis of pore structure in clay due to freeze-thaw. *Case Stud. Constr. Mater.* **2023**, *19*, e02273. [CrossRef]
33. *ASTM D4647/D4647M-13(2020)*; Standard Test Method for Identification and Classification of Dispersive Clay Soils by the Pinhole Test. ASTM International: West Conshohocken, PA, USA, 2020.

34. *ASTM D6572-21*; Standard Test Methods for Determining Dispersive Characteristics of Clayey Soils by the Crumb Test. ASTM International: West Conshohocken, PA, USA, 2021.
35. *ASTM D2487-17(2025)*; Standard Practice for Classification of Soils for Engineering Purposes (Unified Soil Classification System). ASTM International: West Conshohocken, PA, USA, 2025.
36. *GB/T 50123-2019*; Standard for Geotechnical Testing Method. China Architecture & Building Press: Beijing, China, 2019. (In Chinese)
37. *ASTM D2216-19*; Standard Test Methods For Laboratory Determination of Water (Moisture) Content of Soil and Rock by Mass. ASTM International: West Conshohocken, PA, USA, 2019.
38. *ASTM D4318-17e1*; Standard Test Methods for Liquid Limit, Plastic Limit, and Plasticity Index of Soils (Withdrawn 2026). ASTM International: West Conshohocken, PA, USA, 2017.
39. *ASTM D698-12(2021)*; Standard Test Methods for Laboratory Compaction Characteristics of Soil Using Standard Effort (12,400 ft-lbf/ft3 (600 kN-m/m^3)). ASTM International: West Conshohocken, PA, USA, 2021.
40. *ASTM D6035/D6035M-19*; Standard Test Methods for Determining the Effect of Freeze-Thaw on Hydraulic Conductivity of Compacted or Intact Soil Specimens Using a Flexible Wall Permeameter. ASTM International: West Conshohocken, PA, USA, 2019.
41. *ASTM D560/D560M-16*; Standard Test Methods for Freezing and Thawing Compacted Soil-Cement Mixtures. ASTM International: West Conshohocken, PA, USA, 2016.
42. Li, S.; Deng, P. Experimental Study of Shear Strength of Loess under Freeze-thaw Cycles. *Front. Sci. Eng.* **2024**, *4*, 16–23. [CrossRef]
43. Zhou, Z.; Ma, W.; Zhang, S.; Mu, Y.; Li, G. Effect of freeze-thaw cycles in mechanical behaviors of frozen loess. *Cold Reg. Sci. Technol.* **2018**, *146*, 9–18. [CrossRef]
44. Qu, Y.; Chen, G.; Niu, F.; Ni, W.; Mu, Y.; Luo, J. Effect of freeze-thaw cycles on uniaxial mechanical properties of cohesive coarse-grained soils. *J. Mt. Sci.* **2019**, *16*, 2159–2170. [CrossRef]
45. Bao, W.; Wu, Q.; Qin, C.; Hou, T. Mechanical properties of Ili salinized loess under freeze-thaw conditions. *Chin. J. Rock Mech. Eng.* **2024**, *43*, 1775–1787. (In Chinese) [CrossRef]
46. Liu, K.; Ye, W.-J.; Jing, H.-J.; Duan, X.; Zhang, J. Microscopic damage identification and macroscopic mechanical response of loess in seasonal frozen areas. *Chin. J. Geotech. Eng.* **2021**, *43*, 192–197. (In Chinese) [CrossRef]
47. Chu, C.; Yang, L.; Cheng, W.; Wang, J.; Wang, X. Triaxial mechanical behaviours of Ili loess after freeze–thaw. *Front. Earth Sci.* **2024**, *12*, 1454629. [CrossRef]
48. Schofield, A.N.; Wroth, P. *Critical State Soil Mechanics*; McGraw-Hill: London, UK, 1968; Volume 310.
49. Leroueil, S.; Vaughan, P.R. The general and congruent effects of structure in natural soils and weak rocks. *Géotechnique* **1990**, *40*, 467–488. [CrossRef]
50. Wood, D.M. *Soil Behaviour and Critical State Soil Mechanics*; Cambridge University Press: Cambridge, UK, 1990.
51. Zhang, Z.-T.; Zhou, G.-M. Investigating the compaction and the mechanical behaviors of coal gangue as subgrade filler and constructing highway subgrade in practice. *Sci. Rep.* **2024**, *14*, 26272. [CrossRef] [PubMed]
52. Yi, F.; Du, C. Triaxial Testing of Geosynthetics Reinforced Tailings with Different Reinforced Layers. *Materials* **2020**, *13*, 1943. [CrossRef] [PubMed]
53. Zhu, R.; Cai, Z.; Huang, Y.; Zhang, C.; Guo, W.; Wang, Y. Effects of wetting-drying-freezing-thawing cycles on mechanical behaviors of expansive soil. *Cold Reg. Sci. Technol.* **2022**, *193*, 103422. [CrossRef]
54. Hu, X.; Chen, M.; Hu, B.; Du, G.; Li, K. Experimental Study on the Mechanical Behavior of Sandy Soil Reinforced by Disposable Face Mask Chips under Different Stress Paths. *Sustainability* **2023**, *15*, 4059. [CrossRef]
55. Cheng, Z.; Cui, G.; Yang, Z.; Gang, H.; Gao, Z.; Zhang, D.; Xi, C. Improvement of the salinized soil properties of fly ash by freeze-thaw cycles: An impact test study. *Sustainability* **2021**, *13*, 2908. [CrossRef]
56. Li, Z.; Yang, G.; Liu, H. The Influence of Regional Freeze–Thaw Cycles on Loess Landslides: Analysis of Strength Deterioration of Loess with Changes in Pore Structure. *Water* **2020**, *12*, 3047. [CrossRef]
57. Orakoglu, M.E.; Liu, J. Effect of freeze-thaw cycles on triaxial strength properties of fiber-reinforced clayey soil. *KSCE J. Civ. Eng.* **2017**, *21*, 2128–2140. [CrossRef]
58. Zhang, Y.-Z.; Dong, Y.-Q.; Wang, J.-Z.; Wang, M.; Cui, Y.-H.; Kou, X.-K. Effects of freeze–thaw cycles on the deformation and microstructure of silt. *Cold Reg. Sci. Technol.* **2025**, *239*, 104605. [CrossRef]
59. Gao, X.; Tian, R.; Yin, T.; Torres, S.A.G.; Lei, L. Pore-scale freezing of a sandy saline soil visualized with micro-computed tomography. *Permafr. Periglac. Processes* **2024**, *35*, 109–124. [CrossRef]
60. Chen, Y.; Jiang, T.; Wang, Q.; Shen, J.; Shan, X.; Liu, P.; Zhao, G. Differential freezing behavior of different pore water types in saline soil and its influence on soil dynamic characteristics. *Eng. Geol.* **2025**, *358*, 108402. [CrossRef]
61. Zhang, X.; Wang, H.; Zhou, B.; He, Y.; Chang, L.; Tong, Y.; Cao, J. Freeze–thaw deterioration resistance and microstructural mechanisms of polyvinyl alcohol fiber–MICP-treated dispersive soils. *J. Rock Mech. Geotech. Eng.* **2026**, *in press*. [CrossRef]
62. Xian, S.; Lu, Z.; Yao, H.; Fang, R.; She, J. Comparative Study on Mechanical Properties of Compacted Clay under Freeze-Thaw Cycles with Closed and Open Systems. *Adv. Mater. Sci. Eng.* **2019**, *2019*, 9206372. [CrossRef]

63. Liu, K.; Wang, X.; Lian, B.; Hu, S.; Wang, D.; Xue, C.; Liu, J.; Ye, X. Triaxial creep characteristics of undisturbed loess under freeze-thaw cycles and its induced landslide mechanism. *Acta Geotech.* **2025**, *20*, 5543–5563. [CrossRef]
64. Konrad, J.-M.; Morgenstern, N.R. A mechanistic theory of ice lens formation in fine-grained soils. *Can. Geotech. J.* **1980**, *17*, 473–486. [CrossRef]

Disclaimer/Publisher's Note: The statements, opinions and data contained in all publications are solely those of the individual author(s) and contributor(s) and not of MDPI and/or the editor(s). MDPI and/or the editor(s) disclaim responsibility for any injury to people or property resulting from any ideas, methods, instructions or products referred to in the content.